Making a Synthesis of FDTD and DGTD Schemes for Computational Electromagnetics

Dinshaw S. Balsara and Jamesina J. Simpson, *Senior Member, IEEE*

***Abstract*—A novel class of discontinuous Galerkin time-domain (DGTD) schemes, invented by the first author, are presented that are capable of globally preserving the constraints that are inherent in Maxwell's equations. The methods share the same Yee-type mesh structure as finite-difference time-domain (FDTD) schemes for computational electrodynamics. Since FDTD schemes also preserve global constraints, the novelty of this work consists of making a synthesis of FDTD and DGTD schemes. While previous DG methods were based on applying identities involving Gauss' law in weak form to the volumetric elements of a mesh, the newer methods are based on applying identities involving Stokes' law in weak form to the facial elements of the mesh. This fundamental paradigm shift is crucial for obtaining the globally constraint-preserving DGTD methods in this paper. The new DGTD methods meet their design accuracies. The more accurate schemes are indeed more accurate even at the lowest resolutions. Moreover, as the mesh is refined, the schemes reach their design accuracies much faster. These benefits are all attributable to the subcell resolving ability of the DGTD schemes presented here. The higher order methods offer the lowest time to solution, especially when very high accuracies are demanded. Excellent scalability is also demonstrated.**

***Index Terms*—Computational electromagnetics, discontinuous galerkin time-domain (DGTD), electromagnetic propagation, finite-difference time-domain (FDTD), finite volume time-domain (FVTD).**

I. INTRODUCTION

MAXWELL'S equations comprise the foundation of computational electrodynamics (CED). The accurate solution of Maxwell's equations is vital to science and engineering endeavors involving electromagnetic waves across the spectrum, ranging from ultralow frequencies (where geophysical electrodynamic phenomena interact with Planet Earth at multimegameter length scales), to hundreds of terahertz (where visible light interacts with complex material structures at nanometer length scales). Example of scientific and engineering endeavors include: understanding the effects (and mitigation thereof) of solar storms upon power grids; further reductions of the radar cross-section of military platforms; improvements in wireless communications and sensing by incorporating millimeter wave and terahertz technologies; sophisticated first-principles analysis and design of nanoscale plasmonics-based technologies for ultrafast optical computers and ultra-efficient photovoltaics; and even the development of novel optical microscopy techniques to reliably detect deadly human cancers at the earliest possible stage.

The finite-difference time-domain (FDTD) method [1]–[5] has been one of the leading methods in CED for over half a century. FDTD relies on the staggering of the components of the electric and magnetic field vectors, which provides a direct interpretation of the two curl-type equations given by Faraday's Law and the generalized Ampere's Law.

Maxwell's equations are a hyperbolic system, and there have been significant advances in the numerical solution of hyperbolic systems in the last few decades. A very incomplete list of advances that are relevant to CED include [6]–[13]. Some of these methods are based on finite volume (FV) approaches, they are often referred to as finite volume time-domain (FVTD) methods. Discontinuous Galerkin time-domain (DGTD) methods may be viewed as extensions of FVTD methods and provide another approach to attaining high-order accuracy.

Perhaps the best motivation for making such a synthesis of the best aspects of FDTD and FVTD/DGTD is provided by a quick example. Fig. 1(a) shows a cylindrical annulus with an inner radius of 0.15 and an outer radius 0.25 that is set up on a 2-D Cartesian mesh spanning $[-0.5, 0.5] \times [-0.5, 0.5]$ and having 250×250 zones. The permittivity in the ring is 10 times larger than the exterior, as shown in Fig. 1(a). Electromagnetic radiation with a wavelength of 0.1 is allowed to impinge on the ring from the left. Fig. 1(b) and (c) shows the x- and y-components of the electric displacement and Fig. 1(d) shows the z-component of the magnetic induction after the incident radiation has crossed the computational domain five times. Because the interior of the ring acts as a resonant cavity, and because of total internal refraction at the inner boundary of the ring, there are plenty of opportunities for resonances to build up. Fig. 1(b)–(d) shows results from a fourth-order, face-centered FVTD scheme (i.e., primal variables located on the faces of each grid cell) that preserves the divergence constraint; i.e., the divergence is held down to machine precision. We see the formation of all the anticipated resonances in the interior of the ring and the evidence for total internal refraction on the shadow side of the ring.

Manuscript received September 14, 2019; revised January 20, 2020 and May 8, 2020; accepted June 7, 2020. Date of publication June 12, 2020; date of current version June 30, 2020. This work was supported in part by the National Science Foundation under Award NSF-ECCS-19-04774, Award NSF-ACI-1533850, Award NSF-DMS-1622457, Award NSF-ACI-1713765, and Award NSF-DMS-1821242. *(Corresponding author: Jamesina J. Simpson.)*

Dinshaw S. Balsara is with the Department of Physics, Notre Dame University, Notre Dame, IN 46556 USA (e-mail: dinshaw.s.balsara.1@nd.edu).

Jamesina J. Simpson is with the Electrical and Computer Engineering Department, University of Utah, Salt Lake City, UT 84112 USA (e-mail: jamesina.simpson@gmail.com).

Digital Object Identifier 10.1109/JMMCT.2020.3001910

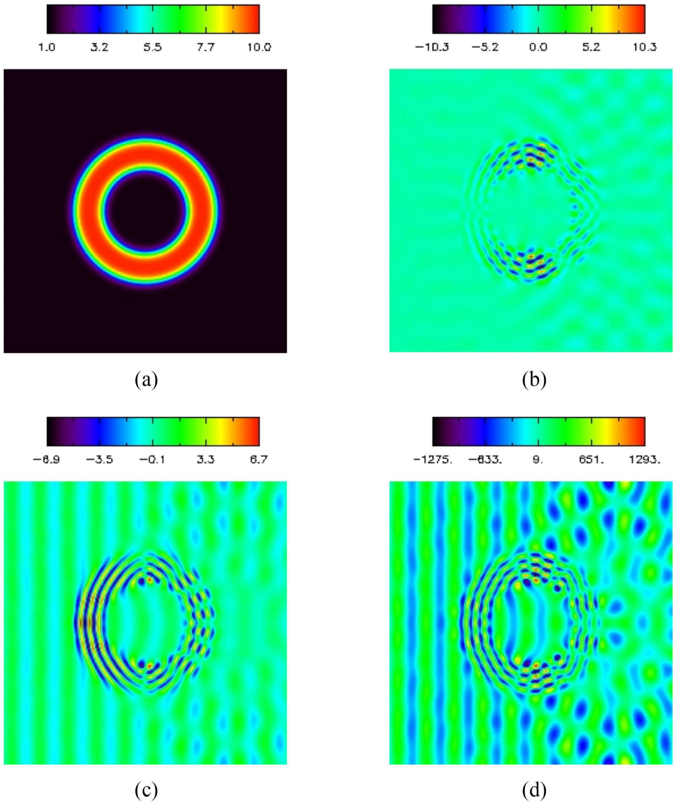

Fig. 1. (a) Schematic of the dielectric annulus. (b) Face-centered, fourth-order accurate FVTD results for the x-direction component of the electric displacement after the electromagnetic radiation impinging from the left on the dielectric annulus traverses the domain five times. (c) Same as (b) but for the y-direction component of the electric displacement. (d) Same as (b) but for the z-direction component of the magnetic induction.

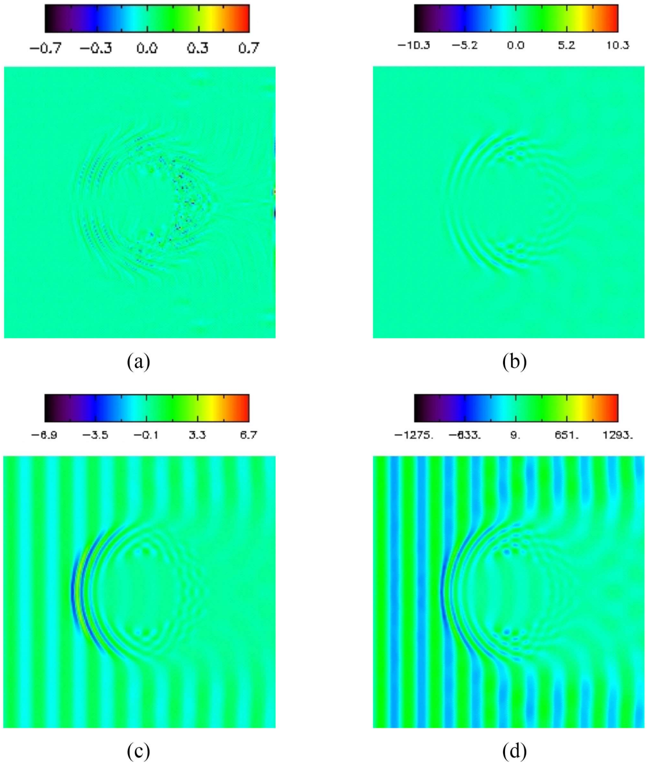

Fig. 2. Same problem as in Fig. 1, but solved using a grid cell-centered, second-order accurate FVTD scheme. (a) Divergence in the electric displacement at the end of the simulation. (b) Results for the x-direction component of the electric displacement after the electromagnetic radiation impinging from the left on the dielectric annulus traverses the domain five times. (c) Same as (b) but for the y-direction component of the electric displacement. (d) Same as (b) but for the z-direction component of the magnetic induction.

Fig. 2 shows the same simulation, on the same mesh, but this time using a grid cell-centered, second-order scheme that is free to build up divergence in the electric displacement (i.e., primal variables located on the cell-centers of each grid cell). Fig. 2(a) shows the fractional divergence that is built up (i.e., the undivided discrete divergence divided by the magnitude of the field in the grid cell of interest and its immediate neighbors). The divergence is seen to reach as much as 60% and is concentrated in exactly those regions of the simulation where the results are the most interesting. Increasing the resolution does not cause the divergence to diminish in magnitude. Fig. 2(b) and (c) shows the x- and y-components of the electric displacement and Fig. 2(d) shows the z-component of the magnetic induction at the same time as in Fig. 1. The color table is the same across Figs. 1 and 2 to facilitate a direct comparison.

Comparing the results in Figs. 1 and 2, the lower order scheme of Fig. 2 fails to capture much of the wave resonance within the annulus; neither does it capture the total internal reflection on the shadow side of the annulus. This shows the value of having a higher order scheme that exactly preserves the divergence constraint. In other numerical experiments, it can be shown that even a very high-order grid cell-centered scheme that is not designed to be divergence-free from the ground-up will build up as much divergence as in Fig. 2(a). (It is important to understand that if this electric field is used in a plasma physics problem, this divergence can cause unphysical electric forces via Gauss' Law.) In other words, the desideratum is a high order of accuracy in conjunction with constraint preservation. That is indeed the motivation of this article that synthesizes FDTD, which has optimal preservation of global constraints, with FVTD and DGTD, which offer high orders of accuracy.

While FVTD schemes reconstruct all the higher order moments of the primal variables, DGTD schemes take all these higher order moments and endow them with time-evolution based on the governing equations. Therefore, it is widely believed that increasingly higher order DGTD schemes might become almost spectrally accurate in their ability to propagate electromagnetic radiation. However, previous generations of DGTD schemes for CED were not globally constraint-preserving (meaning Gauss' Laws were not simultaneously satisfied throughout the computational grid; violating these constraints results in a loss of fidelity with Maxwell's equations) [14]–[23]. There have been, however, a few exceptions where curl- and div-conforming vector bases were used [24]–[26], and we will compare and contrast our methods with them later. For now, we point out that in [25] and [26] the computational domain is divided up into multiple regions so that the FDTD method is used in regions where FDTD is more advantageous and the finite element time-domain or the spectral element time-domain methods are used in other regions, particularly to discretize complicated geometries provides. On the other hand, the *goal* of this article is to introduce a synthesis between FDTD and DGTD methods for CED that includes the advantages of both.

An examination of FDTD and DGTD methods shows they have mutually complementary strengths and weaknesses.

1) Because of the staggered arrangement of the electric and magnetic field vector components in the Yee mesh, FDTD globally preserves the divergence constraints. While some efforts have been made to locally preserve constraints within each element, DGTD methods do not globally preserve constraints.
2) At least when material media are present, FDTD is restricted to second-order accuracy, whereas DGTD can extend to higher orders of accuracy even in the presence of material media.
3) FDTD schemes operate with a robust Courant-Friedrichs-Lewy (CFL) limit, whereas DGTD schemes with increasing order of accuracy suffer from a diminishing CFL.
4) FDTD schemes exhibit substantial numerical dispersion, whereas higher order DGTD schemes can minimize dispersion.
5) FDTD schemes do not incorporate the physics of wave propagation, whereas DGTD schemes closely incorporate the hyperbolic system and include the physics of wave propagation.
6) FDTD schemes are blindingly fast; whereas DGTD schemes are much slower, though efficient use of GPUs may offset this imbalance.
7) FDTD schemes do not accommodate complex geometries very well, whereas DGTD schemes do.

The previous seesaw of mutually complementary strengths and weaknesses in the points above suggest that a cross-fertilization of ideas, and a synthesis of strengths, is highly desirable. The first author of this article has led a sequence of articles in recent years that shows that such a synthesis has emerged [27]–[33]. Most of these advances have been cataloged in the *Journal of Computational Physics*, with the result that they may not be familiar to electrical engineers engaged in CED work.

The twin purposes of this article are: first, to make a synthesis between FDTD and DGTD methods and second, to point to the literature while showing engineers how this synthesis has been affected via the simplest examples. The foundational innovations on which these advances are based are also documented, since many of these innovations were initially made in the field of magnetohydrodynamics (MHD) [34] and have since been engrafted into the field of CED. Some of these ideas are very novel to CED and so, by necessity, this article is designed to be light and intuitive. However, it points to more mathematical detail in the cited literature.

Section II introduces the two important building blocks of the new constraint-preserving DGTD schemes. Section III provides details of the first building block, which is the constraint-preserving reconstruction of the vector fields in CED (meaning Gauss' Laws are satisfied and used to generate the vector fields within each grid cell). Section IV describes the second building block, which is the multidimensional Riemann solver for CED. Section V shows how the two building blocks are combined to obtain globally constraint-preserving DGTD schemes. Section VI discusses higher order time-stepping and presents the dissipation and dispersion properties of the resulting DGTD schemes. Section VII presents some results and Section VIII concludes this article.

II. OVERVIEW OF THE CONSTRAINT-PRESERVING DGTD SCHEMES FOR CED

Maxwell's equations consist of a pair of curl-type, time-evolutionary, hyperbolic partial differential equations (PDEs) and a pair of constraints. The full equation set is written as

$$\frac{\partial \mathbf{D}}{\partial t} - \nabla \times \mathbf{H} = -\mathbf{J} \tag{1a}$$

$$\frac{\partial \mathbf{B}}{\partial t} + \nabla \times \mathbf{E} = 0 \tag{1b}$$

$$\nabla \cdot \mathbf{D} = \rho_E \tag{1c}$$

$$\nabla \cdot \mathbf{B} = 0. \tag{1d}$$

Equations (1a) and (1b) are the time-dependent Ampere's and Faraday's laws with curl operators on the magnetic and electric field intensities, **H** and **E**, respectively. Equations (1c) and (1d) are the Gauss' Law constraints on the electric and magnetic flux densities, **D** and **B,** which constitute the primal variables of the new method. The first two equations ensure that if the latter two constraint equations are satisfied at the initial time, they are satisfied forever. Thus, CED has two constraints, (1c) and (1d), which are linear in the primal variables. The system is closed by the constitutive relations $\mathbf{D} = \varepsilon \mathbf{E}$ and $\mathbf{B} = \mu \mathbf{H}$ and also $\mathbf{J} = \sigma \mathbf{E}$, where ε is the material permittivity, μ is the permeability and σ is the conductivity.

Fig. 3(a) shows the arrangement of primal variables (taken to be **H** and **E**) on a staggered pair of control volumes in FDTD. Fig. 3(a) therefore illustrates why FDTD is constraint-preserving. Fig. 3(b) shows an alternative arrangement of primal variables (taken to be **D** and **B**) on the *same* control volume in the new, globally constraint-preserving FVTD and DGTD schemes. In more pedestrian language, Fig. 3(a) and (b) shows one pair of staggered cells of FDTD and one cell of the newly proposed DGTD schemes, respectively.

The arrangement of variables in Fig. 3(b) could also preserve the global constraints on the FV shown. It does so because the constraints are linear in the choice of primal variables. A beneficial aspect of this choice of primal variables is that the constraints are satisfied even if there are spatially-varying material properties. However, the arrangement of variables in Fig. 3(b) introduces nuances that are addressed in the next two paragraphs.

First, note that the placement of primal variables in Fig. 3(b) is different from FDTD and also different from the traditional DGTD schemes. In a traditional DGTD scheme for CED, one would place the primal variables at the center of the grid cell. This may seem reasonable because Maxwell's equations are

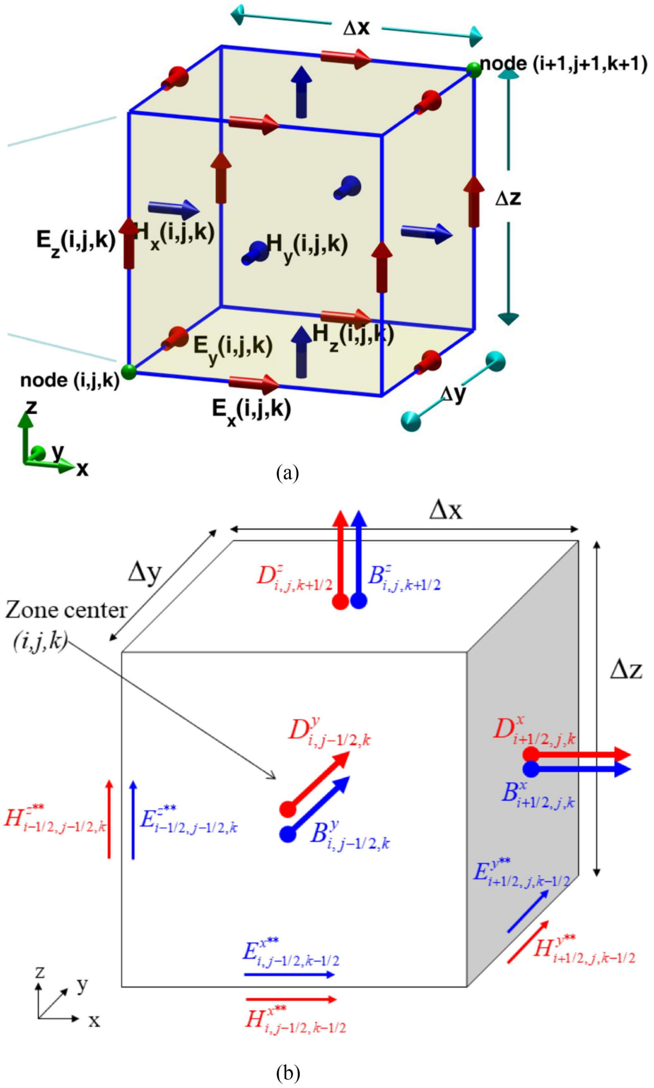

(b)

Fig. 3. (a) Grid-cell arrangement (Yee scheme) for the FDTD scheme. ***H*** and ***E*** fields are the primal variables. (b) Grid-cell arrangement for FVTD, DGTD, or PNPM schemes (courtesy of [28]). The *D* and *B* flux densities through each face of the cubic grid cell are the primal variables. The *x*, *y*, and *z* superscripts on the *D* and *B* flux densities denote the direction of the flux through the *x*, *y*, and *z* faces / sides of the grid cell. The $**$ superscripts on the ***E*** and ***H*** fields along the edges of the grid cell are in reference to the strongly interacting state between grid cells and are explained in Section IV. They are obtained from a multidimensional Riemann solver.

3-D and having all the variables at the same location permits the exploitation of the 3-D gradients [10]–[13], [15]. However, following traditional DGTD schemes too closely does not yield a globally constraint-preserving scheme – i.e., a scheme that satisfies the discrete constraints for each grid cell as well as satisfying the constraints pointwise at each location within each grid cell.

For the new constraint-preserving DGTD scheme, the collocation of variables in Fig. 3(b) is preferred. But if the components of the electric displacement and magnetic induction fields are colocated at the faces of the mesh, then a strategy is needed for retrieving these variables within the interior of the control volume shown in Fig. 3(b). (In other words, the time-evolution of the PDE relies on 3-D gradients, therefore the vector fields for the primal variables must be represented three-dimensionally.) Furthermore, the retrieval of these variables within the interior of the control volume must be done in a fashion that fully respects the constraints in (1c) and (1d). In other words, we need a *constraint-preserving reconstruction of vector fields*. Such a constraint-preserving reconstruction of the vector fields forms the *first important building block* of the globally constraint-preserving DGTD schemes discussed here. It will be presented in detail in Section II.

To introduce the second building block, the CED equations form a hyperbolic system that are written in the following flux form (the subscripts denote the Cartesian orientation of the corresponding component):

$$\frac{\partial}{\partial t}\begin{pmatrix} D_x \\ D_y \\ D_z \\ B_x \\ B_y \\ B_z \end{pmatrix} + \frac{\partial}{\partial x}\begin{pmatrix} 0 \\ B_z/\mu \\ -B_y/\mu \\ 0 \\ -D_z/\varepsilon \\ D_y/\varepsilon \end{pmatrix} + \frac{\partial}{\partial y}\begin{pmatrix} -B_z/\mu \\ 0 \\ B_x/\mu \\ D_z/\varepsilon \\ 0 \\ -D_x/\varepsilon \end{pmatrix} + \frac{\partial}{\partial z}\begin{pmatrix} B_y/\mu \\ -B_x/\mu \\ 0 \\ -D_y/\varepsilon \\ D_x/\varepsilon \\ 0 \end{pmatrix} = \begin{pmatrix} -\sigma\left(D_x/\varepsilon\right) \\ -\sigma\left(D_y/\varepsilon\right) \\ -\sigma\left(D_z/\varepsilon\right) \\ 0 \\ 0 \\ 0 \end{pmatrix}. \tag{2}$$

Note that the *x*-flux mediates the propagation of electromagnetic waves in the *x*-direction. Similarly, the *y*- and *z*-fluxes mediate the propagation of electromagnetic waves in the *y*- and *z*-directions, respectively. The characteristic matrix derived from the *x*-flux provides the eigenvalues (wave speeds) and eigenvectors (which provide the correct polarization of the waves that propagate in the *x*-direction). The characteristic matrices from the *y*- and *z*-fluxes provide analogous information for the wave speeds and eigenvectors for the *y*- and *z*-directions, respectively. Note that the second and fifth components of the *x*-flux are equal and opposite to the first and fourth components of the *y*-flux. Other symmetries are apparent in (2).

Examining Fig. 3(b), to have a constraint-preserving update, E_z and H_z at the *z*-directed edges of the grid cell must be uniquely specified. However, if the waves are propagating in the *x*-direction, then E_z and $H_z$should be chosen from the *x* -flux. And, if the waves are propagating in the *y*-direction then E_z and $H_z$should be chosen from the *y*-flux. Which choice is correct? The answer is that in a full 3-D computation a priori knowledge of the wave propagation direction is not known. Therefore, the correct answer is that we should use a *multidimensional Riemann solver* (see Section IV) to obtain E_z and H_z. The multidimensional Riemann solver resolves the correct wave propagation in the general case. The multidimensional Riemann solver forms the *second important building block* of the globally constraint-preserving DGTD schemes discussed here. It will be discussed in detail in Section III.

With these two building blocks in place, we are ready to get our first glimpse of the difference between a traditional DG scheme and the new, globally constraint-preserving DGTD scheme. The difference is fundamental because it pertains to the very starting point from which the schemes are formulated. Traditional DG schemes start from the conservation law in (2) which has a divergence form. As a result, the resulting scheme can never retrieve the constraints inherent in the curl form in (1). Earlier generations of DGTD [15] derive from such a starting point. In the design of traditional DG schemes, one then applies Gauss' Theorem to (2), viewed volumetrically, thereby relinquishing all hope of global constraint preservation from the very onset. The novel DGTD schemes presented here derive from the more natural curl form that is inherent in (1) for Maxwell's equations. The formulation respects the fact that Stokes law lives on manifolds (surfaces). Therefore, within the *x*-faces of Fig. 3(b), Stokes' theorem can be applied to the *x*-component of the evolutionary equations. Similar treatment is given to the *y*- and *z*-faces. If the electric and magnetic fields are uniquely specified at the edges of the cell in Fig. 3(b) (which is possible thanks to our two building blocks) then the constraint preservation in FDTD [see Fig. 3(a)] is also retrieved in our new DGTD [see Fig. 3(b)]. It is by matching the correct mathematical theorem (Stokes theorem) to the curl form of Maxwell's equations that our new DGTD scheme retains the advantages that are inherent in the physics of Maxwell's equations, (1). Such a program plan for globally constraint-preserving DG schemes has been evolved for MHD [31], [32], [35], [36]. This will be discussed in detail in Section IV. The resulting DGTD schemes, especially at higher orders, have extremely low dissipation and dispersion and robust CFL numbers as shown in [31] and [33]. We present some of the most prominent results from that work in Section V.

III. FIRST BUILDING BLOCK: CONSTRAINT-PRESERVING RECONSTRUCTION OF VECTOR FIELDS FOR CED

Details of the constraint-preserving reconstruction of the vector fields are now provided. For simplicity, a 2-D mesh is considered. The goal is to retain the divergence-free constraint for the magnetic induction [see (1d)]. Fig. 4(a) schematically shows a first-order accurate, constraint-preserving specification of the magnetic induction components on the faces on the sides of one grid cell (*x*- and *y*-sides of the shaded square since there is no variation in the *z*-direction). The components have constant values, making them first-order accurate. Let B_x^+ and B_x^- denote the *x*-components of the magnetic induction at the right and left *x*-faces of the shaded grid cell in Fig. 4(a). Let B_y^+ and B_y^- denote the *y*-components of the magnetic induction at the top and bottom *y*-faces of the shaded grid cell. If the dimensions of the grid cell are Δx and Δy in the *x*- and *y*-directions, the discrete divergence-free constraint applied to the whole grid cell is written as $(B_x^+ - B_x^-)\Delta y + (B_y^+ - B_y^-)\Delta x = 0$. Thus, the boundaries of the grid cell in Fig. 4(a) contain only three independent pieces of information, since the fourth facial component may always be satisfied by invoking the constraint equation.

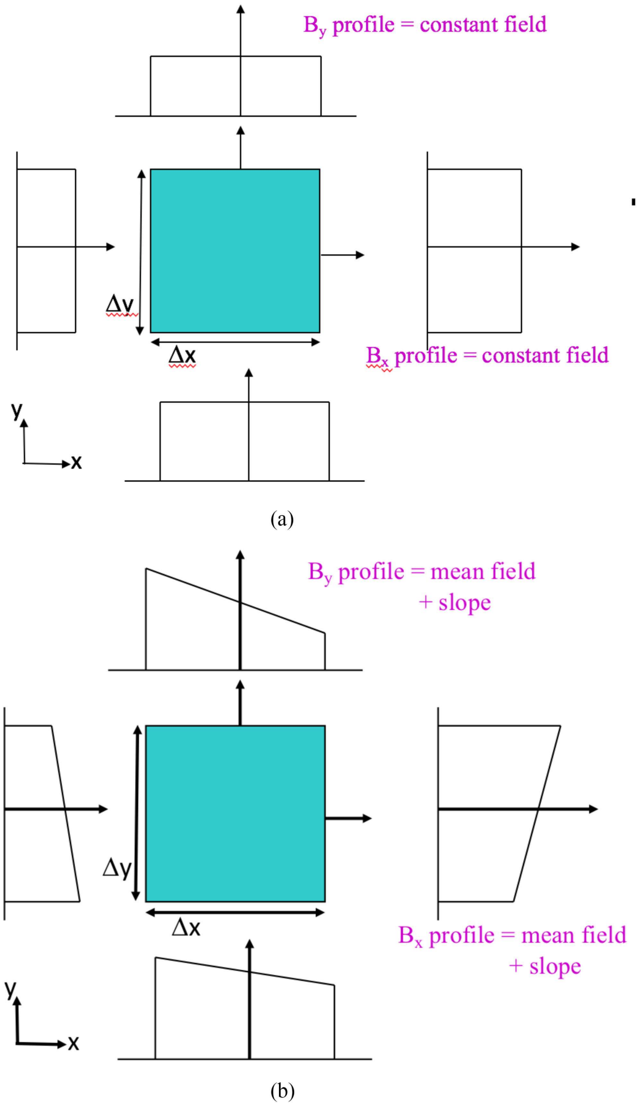

(a)

(b)

Fig. 4. Horizontal *xy*-slice of the grid cell of Fig. 3(b) (depicted as a shaded square). Profiles for the *B* flux densities through each face (side) of the cubic grid cell are shown. (a) First-order accurate profiles on each face (*x*- and *y*-sides of the grid cell) are assumed to be constant and constraint-preserving. (b) Second-order accurate, constraint-preserving profiles on each face (*x*- and *y*-sides of the grid cell) are assumed to vary linearly along each side.

For our purposes, the constraint-preserving reconstruction is the act of starting with the limited information in the faces of Fig. 4(a) and using it to obtain the field in the entire interior of the grid cell. For first-order accurate reconstruction, it is important to specify the magnetic induction over the entire shaded cell in such a way that it continuously matches the constant profiles along all of the faces on the sides of the grid cells. This is achieved by the following [mean fields + slopes, as labeled in Fig. 4(b)]:

$$B_x(x,y) = a_0 + a_x x \quad B_y(x,y) = b_0 + b_y y. \tag{3}$$

The divergence constraint, applied in differential form is then written as

$$\partial_x B_x(x,y) + \partial_y B_y(x,y) = a_x + b_y = 0. \tag{4}$$

Taking $(x, y) = (0, 0)$ to be at the center of the cell, yields

$$\begin{aligned} a_0 &= \left(B_x^+ + B_x^-\right)/2;\ a_x = \left(B_x^+ - B_x^-\right)/\Delta x \\ b_0 &= \left(B_y^+ + B_y^-\right)/2;\ b_y = \left(B_y^+ - B_y^-\right)/\Delta y. \end{aligned} \tag{5}$$

It turns out that $a_x + b_y = 0$ is exactly equivalent to the discrete divergence constraint. However, (3) is only first-order accurate because $B_x(x, y)$ lacks linear variation in the *y*-direction and $B_y(x, y)$ lacks linear variation in the *x*-direction.

Fig. 4(b) schematically illustrates how a constraint-preserving, specification may be extended to second-order accuracy by allowing the components of the magnetic induction to vary linearly in a direction transverse to the corresponding face on the side of the grid cell. Again, for our purposes, the constraint-preserving reconstruction is the act of starting with the limited information in the faces of Fig. 4(a) and using it to obtain the field in the entire interior of the grid cell; but this time we do it with second-order accuracy. Again, it is important to specify the magnetic induction over the entire shaded grid cell in such a way that it continuously matches the linear profiles along all of the faces on the sides of the grid cell. Let $B_x^+ + (\Delta_y B_x^+)(y/\Delta y)$ and $B_x^- + (\Delta_y B_x^-)(y/\Delta y)$ denote the linear profiles for the *x*-components of the magnetic induction on the right and left *x*-faces on the sides of the shaded grid cell in Fig. 4(b); notice that they vary linearly in the *y*-direction. Let $B_y^+ + (\Delta_x B_y^+)(x/\Delta x)$ and $B_y^- + (\Delta_x B_y^-)(x/\Delta x)$ denote the linear profiles for the *y*-components of the magnetic induction on the top and bottom *y*-faces of the shaded grid cell; notice that they vary linearly in the *x*-direction. The specification within the cell should be second-order accurate and should satisfy the divergence-free aspect inherent in the Gauss' law constraint.

Initially, it may seem that there are eight independent pieces of information at the faces on the sides of the grid cell shown in Fig. 4(b) (four mean values for the field components and four slopes). However, the mean values are not independent. They are related by the discrete divergence constraint. As a result, the faces on the sides of the grid cell in Fig. 4(b) actually have seven independent pieces of information. To reconstruct components in the interior that match the values along the faces on the sides of the grid cell, polynomials of the following form are inadequate:

$$\begin{aligned} B_x(x, y) &= a_0 + a_x x + a_y y \\ B_y(x, y) &= b_0 + b_x x + b_y y. \end{aligned} \tag{6}$$

The reason is, after applying the divergence constraint in (4), the above-mentioned polynomials only have five truly independent coefficients. With these five coefficients, the seven independent pieces of information will not be matched at the faces on the sides of the grid cell. Thus, the polynomials should be enriched. It turns out the following second-order polynomials are appropriate:

$$\begin{aligned} B_x(x, y) &= a_0 + a_x x + a_y y + a_{xx} x^2 + a_{xy} xy \\ B_y(x, y) &= b_0 + b_x x + b_y y + b_{xy} xy + b_{yy} y^2. \end{aligned} \tag{7}$$

Equation (7) has ten coefficients, however, not all of them are independent as is seen by applying the constraint in the differential form to the above-mentioned equations:

$$\begin{aligned} &\partial_x B_x(x, y) + \partial_y B_y(x, y) = 0 \Rightarrow \\ &a_x + b_y = 0;\ 2a_{xx} + b_{xy} = 0;\ a_{xy} + 2b_{yy} = 0. \end{aligned} \tag{8}$$

Out of the ten coefficients in (7), only seven are independent after taking into account the three constraint equations in (8). Therefore, the number of truly independent coefficients in the reconstruction exactly matches the number of independent pieces of information contained on the faces on the sides of the grid cell of Fig. 4(b). Matching the polynomials in the interior from (7) to the linear variation along the faces on the sides of the grid cell yields an exact solution for these coefficients:

$$\begin{aligned} a_0 &= ({B^+}_x + {B^-}_x)/2 - a_{xx}\Delta x^2/4; a_x = ({B^+}_x - {B^-}_x)/\Delta x \\ a_y &= (\Delta_y {B^+}_x + \Delta_y {B^-}_x)/(2\Delta y) \\ a_{xx} &= -(\Delta_x {B^+}_y - \Delta_x {B^-}_y)/(2\Delta x \Delta y); a_{xy} = -2b_{yy} \\ b_0 &= ({B^+}_y + {B^-}_y)/2 - b_{yy}\Delta y^2/4; \\ b_x &= (\Delta_x {B^+}_y + \Delta_x {B^-}_y)/(2\Delta x) \\ b_y &= ({B^+}_y - {B^-}_y)/\Delta y \\ b_{yy} &= -(\Delta_y {B^+}_x - \Delta_y {B^-}_x)/(2\Delta x \Delta y); b_{xy} = -2a_{xx}. \end{aligned} \tag{9}$$

This completes our description of the constraint-preserving reconstruction of vector fields. Recall that we started with the facial information for the vectorial components in Fig. 4(b) and obtained the entire vector field in (7) and (9) in a fashion that satisfies the constraint at all points, (8). Because we retained the linear variation in the faces, this is a second-order accurate reconstruction.

There is a wealth of content along these lines in the literature. Constraint-preserving reconstruction strategies for vector fields were first invented within the context of MHD [37]–[41] and then transported over to CED [27]–[31]. Balsara and Dumbser [40] showed that these ideas extend to unstructured tetrahedral meshes at high orders. Balsara *et al.* [42] showed that these ideas work even for isoparametrically mapped, boundary-conforming meshes, also at high orders. Balsara *et al.* [27]–[29] extended these ideas to include Gauss' law for the electric displacement constraint equation in (1c) and [32] showed that these ideas work within the context of globally constraint-preserving DGTD schemes for CED. For the sake of completeness, it is also worth pointing out that these high-order reconstruction strategies were inspired by allied work in higher order schemes [43]–[45].

For the interested reader, there are additional computational costs resulting from the constraint-preserving reconstruction. However, the constraint-preserving reconstruction adds only $\sim 5\%$ to the cost of the algorithm. This is because all the linear algebra that needs to be done to enforce the linear divergence-constraints has indeed been done analytically and it has been documented in several articles [27]–[29], [39].

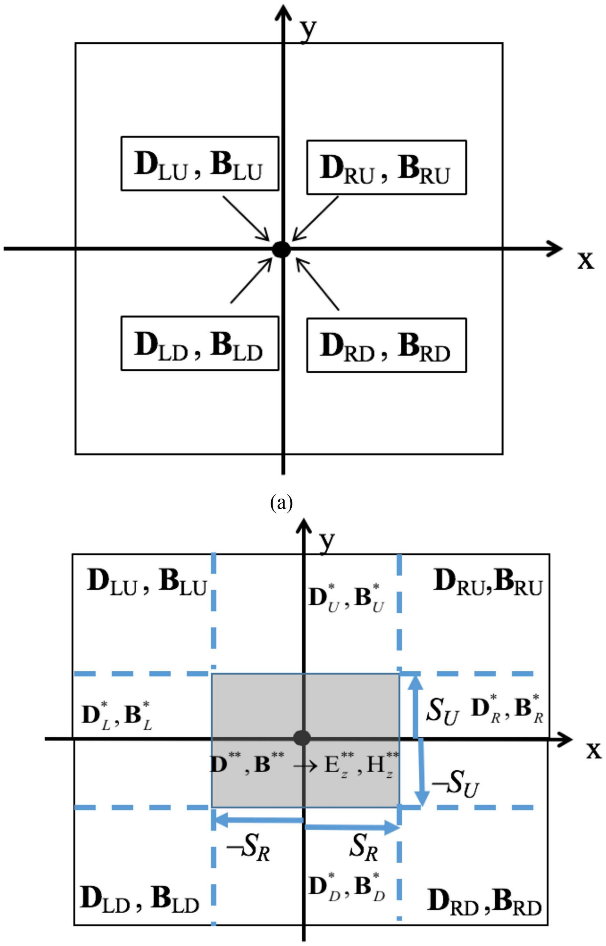

(a)

(b)

Fig. 5. (a) Four grid cells in an xy-plane of a 3-D grid that converge at the z-directed edge shared by the four grid cells. The z-directed edge is indicated by the center black dot, and the four abutting grid cells are shown as four squares. The four states have subscripts given by "RU" for right-upper; "LU" for left-upper; "LD" for left-down, and "RD" for right-down. The situation before the four states start interacting is shown. The arrows indicate that higher order reconstruction within each of the four grid cells is used to obtain the four input states along the z-edge. (b) Same situation as in (a), but after the four states start interacting with each other. Four 1-D Riemann problems, bounded by dashed lines and labeled with single-starred states (components with $*$ superscripts), develop (expand outward in the direction of the arrows). The shaded region with the double-starred states (components with $**$ superscripts) depicts the strongly interacting state that arises when the four 1-D Riemann problems interact with one another. Courtesy of [28].

IV. SECOND BUILDING BLOCK: MULTIDIMENSIONAL RIEMANN SOLVERS FOR CED

A Riemann problem is an initial value problem comprised of a conservation equation along with piecewise initial data that has a discontinuity in the domain of interest (here, between grid cells). Although the Riemann problems in the grid evolve over time, initially the 1-D Riemann problems exist along the faces between two grid cells and multidimensional Riemann problems exist along the edges of grid cells bordering multiple grid cells. The multidimensional Riemann problem was first studied within the context of computational fluid dynamics (CFD) in [46]. Since CFD is just another prototypical hyperbolic system, as are Maxwell's equations, the insights drawn in CFD are transportable to Maxwell's equations.

A multidimensional Riemann problem is formed when four states (expressions) for a component converge at the edges of multiple grid cells. Fig. 5(a) shows four states for the D and B components that converge at a z-directed edge shared by four grid cells. The four states are labeled using the following subscripts: RU (for Right-Upper state), LU (for Left-Upper state), LD (for Left-Down state), and RD (for Right-Down state). Four 1-D Riemann problems form naturally between each pair of states, as shown schematically by the four arrows in Fig. 5(b). An x-directional Riemann problem develops between the RU and LU states and between the RD and LD states. Analogously, y-directional Riemann problems develop between the RU and RD states and between the LU and LD states.

A *strongly-interacting state*, appears in the shaded square of Fig. 5(b). In this region, the four 1-D Riemann problems intersect. As time evolves, the 1-D Riemann problems evolve self-similarly, as does the strongly-interacting state. For example, as time evolves, the strong-interacting state, which starts at the center black dot in Fig. 5(a), expands outward over time in the form of the shaded rectangle shown in Fig 5(b).

The study of the multidimensional Riemann problem is devoted to understanding the structure and evolution of the strongly interacting state. In general, not all of the detail in the strongly interacting state must be retained in the computation, however, some approximate cognizance of its existence is very important. Approximate, multidimensional Riemann solvers have been designed to model the essentials of this strongly interacting state. They were first invented within the context of MHD [47]–[54] and then transported over to CED [27]–[33]. By now, such Riemann solvers have been used in the study of nonrelativistic Euler flow; nonrelativistic MHD, relativistic Euler flow, and relativistic MHD; and they work very well for all of those hyperbolic PDE systems. It was, therefore, natural to also draw on these insights for CED, as was done in [27]–[29]. The multidimensional Riemann solver is also referred to as the MuSIC Riemann solver; standing for **Mu**ltidimensional, **S**elf-similar Riemann Solver, based on a strongly **I**nteracting state that is **C**onsistent with the governing hyperbolic law.

The MuSIC Riemann solver is used to obtain the magnetic and electric fields along the edges of the grid cells of a 3-D grid. For example, imagine a 3-D grid comprised of the grid cells shown in Fig. 3(b). In particular, the following components exist along the front-left, z-directed edge of the grid cell in Fig. 3(b): $H^{z^{**}}_{i-1/2,j-1/2,k}$ and $E^{z^{**}}_{i-1/2,j-1/2,k}$. The MuSIC Riemann solver solves for these two components using a physically meaningful understanding of the different directions in which the electromagnetic waves might be propagating. Specifically, the MuSIC Riemann solver takes as input the state values from the four grid cells that surround that z-edge. It returns as output the resolved magnetic and electric fields along that z-edge. Similar considerations apply to the x- and y-edges in Fig. 3(b).

For structured mesh calculations, the MuSIC Riemann solver for CED has been turned into simple plug-and-play technology in of [28, Sec. V] and [32, Appendix C]. For unstructured meshes, Balsara *et al.* [51] and Balsara and Dumbser [52] provide the necessary details about the construction of such MuSIC Riemann solvers. For this reason, further mathematical details are not provided here.

V. FORMULATION OF CONSTRAINT-PRESERVING DGTD SCHEMES

A. *Starting Point for the New Constraint-Preserving DGTD Scheme*

There is a fundamental difference between a traditional DGTD scheme and the new constraint-preserving DGTD scheme. The difference is fundamental because it pertains to the starting point from which each of the two schemes are formulated. The next two paragraphs should be read together and cross-compared to appreciate the parallels as well as the differences between the traditional DGTD and newer DGTD schemes. They are intentionally written in a style that highlights the parallels and yet brings out the differences.

Traditional DGTD is considered first. Traditional DG schemes take the conservation law in (2) as their starting point. A traditional DG scheme for conservation laws is derived from the Gauss law-based vector identity

$$\nabla \cdot (\phi \mathbf{F}) = \phi \nabla \cdot \mathbf{F} + \mathbf{F} \cdot \nabla \phi. \tag{10}$$

The primal variables reside within the volume of each grid cell and are then endowed with higher moments in that same volume. As the space of volumetric moments within each cell is enriched, the scheme becomes more spectrally accurate. These moments are derived from suitable polynomial basis functions (also referred to as trial functions) of increasing order in each cell. It is important to note that the polynomial basis functions reside in the *volume* of the grid cell being considered, since Gauss' Law is also applied to the grid cell volume. By definition, any Galerkin scheme involves a Galerkin projection step. As a result, a set of test functions are chosen in the same cell; these usually coincide with the trial functions in the grid cell. The conservation law in (2) is then projected within each cell on to the space of test functions—this is basically a volumetric convolution of the governing equation with the test functions. Note that the flux form in (2) satisfies Gauss' law and, as a result, Gauss' theorem is used to convert divergences over volumes into area integrals over the faces of the volume. A weak form imposition of the fluxes at the faces, using 1-D Riemann solvers, then completes the scheme. Unfortunately, this is a poor starting point, since a traditional DG scheme will never be globally constraint-preserving.

Now consider the new DGTD scheme. Equation (1) in curl form is taken as the starting point. The primal variables reside on the faces of each grid cell, and they are endowed with higher moments on those faces. Then, Recall that Stokes' law applies to surfaces. As a result, the DG-like scheme for updating curl-type equations is derived from the Stokes Law-based vector identity

$$\nabla \times (\phi \mathbf{D}) = (\nabla \phi) \times \mathbf{D} + \phi \nabla \times \mathbf{D}. \tag{11}$$

Thus, in a 3-D code, the *x*-components of $\mathbf{D}$ and $\mathbf{B}$ will take on higher moments in the *y*- and *z*-directions on the *x*-faces of the grid cells. Similarly, the *y*-components of $\mathbf{D}$ and $\mathbf{B}$ will take on higher moments in the *x*- and *z*-directions on the *y*-faces of the grid cells. Likewise, the *z*-components of $\mathbf{D}$ and $\mathbf{B}$ will take on higher moments in the *x*- and *y*-directions on the same *z*-faces of the grid cells. As the facial moments on the faces of each grid cell is enriched, the scheme becomes more spectrally accurate. These moments are derived from suitable polynomial basis functions (also referred to as trial functions) of increasing order on each face. It is important to note that the polynomial basis functions reside on the *faces* of the grid cell being considered, since Stokes' law is also applied to the grid cell faces. By definition, any Galerkin scheme involves a Galerkin projection step; except that this time the projection is enforced on the faces of Fig. 3(b). As a result, a set of test functions are chosen on the same faces; these usually coincide with the trial functions on the faces. The curl-type update in (1) is then projected on each face on to the space of test functions—this is an areal convolution of the governing equation with the test functions. Note that the curl form in (1) satisfies Stokes' law and, as a result, Stokes' theorem is used to convert curls over facial areas into line integrals over the edges that bound the face; see Fig. 3(b). A weak form imposition of the electric and magnetic field components along the edges that bound the faces, using multidimensional Riemann solvers, then completes the scheme. The electric and magnetic fields along each edge are uniquely defined by the multidimensional Riemann solver in a way that encapsulates the physics of multidimensional wave propagation. This is a better starting point, since such a DG scheme will always be globally constraint-preserving. This will be emphasized in the following text.

The connection between FDTD and the new generation of DGTD schemes is, therefore, tightly established at least at an intuitive level in the previous paragraph. The mathematical details are developed in subsequent parts of this Section. To keep the discussion simple, a second-order, 2-D case is considered. Further details for higher order, globally constraint-preserving DGTD schemes have been explicitly cataloged in [31] and [32].

The method presented here is not a traditional DG scheme for conservation laws. It shares several features with a traditional DG scheme, which is why it is a DG-like scheme. However, it also shares many aspects with an FDTD scheme. Balsara and Käppeli [35, Sec. II] provides a precise comparison and contrast between the DG-like schemes that we formulate here and a traditional DG scheme.

B. *Formulation*

Even though a 2-D scheme is initially of interest, it is most beneficial to realize that (1a) and (1b) are actually 3-D and to consider the DG formulation on a 3-D mesh. Specifically, let us first focus on (1a). One grid cell of a 3-D mesh is shown in Fig. 3(b). The mesh is Cartesian and has uniform grid cells with size Δx, Δy, and Δz in the *x*-, *y*-, and *z*-directions. For simplicity, the grid cell in Fig. 3(b) extends over $[-\Delta x/2, \Delta x/2] \times [-\Delta y/2, \Delta y/2] \times [-\Delta z/2, \Delta z/2]$, although it turns out that Δz does not play a role in the update equations that will be derived. However, since a 2-D scheme will be described, there will only be spatial variations only in the *x*-direction or in the *y*-direction. The focus is also restricted to $\mathrm{TE_z}$ modes.

Let $\hat{\mathbf{n}}$ be the unit outward pointing normal to one grid cell. Let A_n be the area of the face of the grid cell to which $\hat{\mathbf{n}}$ is the unit normal. First take $\hat{\mathbf{n}} = \hat{\mathbf{x}}$ in Fig. 3(b). In that case, the area A_n is the right *x*-face which contains the field component D_x that will be evolved via (1a). Now take $\hat{\mathbf{n}} = \hat{\mathbf{y}}$ in Fig. 3(b); in that case, the area A_n is the upper *y*-face, which contains the field component D_y that we are interested in evolving via (1a). We wish to project (1a) into a space of test functions. The test functions will be identical to the trial functions, which will be explicit. To make the DG-like projection, (1a) is first multiplied by the test function ϕ. Next, the dot product of A_n with the unit normal $\hat{\mathbf{n}}$ to that face is taken. Integrating over that face and using the vector identity in (11) yields

$$\frac{\partial}{\partial t}\left(\int_{A_n}(\hat{\mathbf{n}}\cdot\mathbf{D})\,\phi\, dA_n\right) - \int_{\partial A_n}(\phi\mathbf{H})\cdot d\vec{\ell} + \int_{A_n}\hat{\mathbf{n}}\cdot[(\nabla\phi)\times\mathbf{H}]\, dA_n = -\int_{A_n}\mathbf{J}\phi\, dA_n. \qquad (12)$$

Equation (12) is the first master equation that stems from the extended Ampere’s law. (The $\mathbf{D}$ terms in the above-mentioned equation indicate that these are the facial primal variables; the $\mathbf{H}$ terms are obtained at the edges of the grid cells by application of a multidimensional Riemann solver; the $\mathbf{H}$ terms are obtained within the faces of the grid cells by the application of a 1-D Riemann solver; and the current density within each face is obtained via an implicit treatment of the stiff source terms.) The boundary of the face under consideration is denoted by ∂A_n. The infinitesimal vector $d\vec{\ell}$ in the middle term of (12) runs along ∂A_n and denotes the length of the grid cell. The existence of a unit normal, $\hat{\mathbf{n}}$, lends a right-handed directionality to $d\vec{\ell}$.

Equation (12) provides the desired Galerkin projection strategy; but it is applied to a curl-type equation on the faces of the grid cells. The first term in (12) provides successive moments of the facial primal variable. Note that the second term in (12) is interpreted in a weak form using a multidimensional Riemann solver and is analogous to the flux term in a traditional DG method for conservation laws. The third term in (12) is analogous to the volume term in a traditional DG method for conservation laws. Equation (12) even holds if the face/manifold that is integrated over is curved as long as $\hat{\mathbf{n}}$ is locally normal to the manifold and as long as the test function ϕ resides in that manifold. The next few paragraphs will show how it is to be used to design a DG scheme at the second order.

Applying (12), on the right *x*-face of the grid cell shown in Fig. 3(b), i.e., the face with $x = \Delta x/2$, the second-order accurate evolution of the *x*-component of the electric displacement vector is asserted to be of the form

$$D^x(y,t) = D_0^x(t) + D_y^x(t)\left(\frac{y}{\Delta y}\right). \qquad (13)$$

The *x* superscript indicates the component of the electric flux density. The subscript 0 denotes the mean D_x value on that face. The *y* subscript denotes the direction in which D_x is allowed to vary over time on the *x*-face of the grid cell.

Note that the *z*-variation in the above-mentioned equation has been suppressed because a 2-D scheme is being presented. The trial functions are $\phi(y) = 1$ and $\phi(y) = (y/\Delta y)$. Using $\hat{\mathbf{n}} = \hat{\mathbf{x}}$ and the test function $\phi(y) = 1$, (12) then yields

$$\frac{dD_0^x(t)}{dt} - \frac{1}{\Delta y}\begin{bmatrix} H^{z^{**}}(x=\Delta x/2, y=\Delta y/2) - \\ H^{z^{**}}(x=\Delta x/2, y=-\Delta y/2) \end{bmatrix} = 0. \qquad (14)$$

Using $\hat{\mathbf{n}} = \hat{\mathbf{x}}$ and the test function $\phi(y) = (y/\Delta y)$ in (12) yields:

$$\frac{1}{12}\frac{dD_y^x(t)}{dt} - \frac{1}{2\Delta y}\begin{bmatrix} H^{z^{**}}(x=\Delta x/2, y=\Delta y/2) \\ +H^{z^{**}}(x=\Delta x/2, y=-\Delta y/2) \end{bmatrix} + \frac{1}{\Delta y}\langle H^{z*}(x=\Delta x/2, y)\rangle_{\text{line avg}} = 0. \qquad (15)$$

Equation (12) is crucially important for deriving the above-mentioned two equations. Here, the double-starred $H^{z^{**}}(x = \Delta x/2, y = \Delta y/2)$ and $H^{z^{**}}(x = \Delta x/2, y = -\Delta y/2)$ are magnetic field components that are obtained at two edges of the right *x*-face in Fig. 3(b). They are obtained by applying a 2-D Riemann solver at the edges of the mesh. The factor $(1/12)$ in (15) is the analog of a mass matrix. Because the Cartesian mesh (in this case centered locally in the middle of each grid cell) has orthogonal bases, the mass matrix is diagonal. Also note that the terms within angled brackets, i.e., terms with $\langle\ \rangle$, represent suitably high-order line averages on a face; these terms with an angled bracket should be obtained with a suitably high-order quadrature along the faces of the each grid cell. In this work, since the *z*-variation is suppressed, the well-known 1-D Gauss-Legendre quadrature is used to carry out the facial integrals. 1-D Riemann problems on the right face being considered to furnish the single-starred $H^{z*}(x = \Delta x/2, y)$ component of the magnetic field that is to be used in the angled brackets. These 1-D Riemann problems are solved at each of the quadrature points on the *x*-face.

Using an analogous approach on the back *y*-face of the grid cell shown in Fig. 3(b) (i.e., on the face with $y = \Delta y/2$) yields

$$\frac{1}{12}\frac{dD_x^y(t)}{dt} + \frac{1}{2\Delta x}\begin{bmatrix} H^{z^{**}}(x=\Delta x/2, y=\Delta y/2) \\ +H^{z^{**}}(x=-\Delta x/2, y=\Delta y/2) \end{bmatrix} - \frac{1}{\Delta x}\langle H^{z*}(x, y=\Delta y/2)\rangle_{\text{line avg}} = 0. \qquad (16)$$

Here again, the double-starred $H^{z^{**}}(x = \Delta x/2, y = \Delta y/2)$ and $H^{z^{**}}(x = -\Delta x/2, y = \Delta y/2)$ are magnetic field components that are obtained at the edges of the back *y*-face in Fig. 3(b). They are obtained by the application of a 2-D Riemann solver at the edges of the mesh. 1-D Riemann solvers on the back face being considered furnish the single-starred $H^{z*}(x, y = \Delta y/2)$ component of the magnetic field that is to be used in the angled brackets. These 1-D Riemann problems are solved at each of the quadrature points on the *y*-face. Equation (14) and the analogous equation in the *y*-direction taken together also ensure that the mean electric displacement field components on the faces of the grid cells preserve the constraint-preserving property at a discrete level. In other words, the traditional, globally constraint-preserving, Yee-type update that has always been built into FDTD is retrieved!

Next, consider (1b). Equation (1b) provides the evolution of the z-component of the magnetic induction. This component resides on the z-faces in Fig. 3(b). Because a 2-D formulation is considered, either of the two z-faces in Fig. 3(b) may be chosen. Consider a case where $\hat{\mathbf{n}} = \hat{\mathbf{z}}$ is taken. In that case, the area A_n will be the far z-face which contains the field component B_z that we are interested in evolving via (1b). A procedure is followed that is analogous to the one that provided (12). However, this time the starting point is (1b), yielding

$$\frac{\partial}{\partial t}\left(\int_{A_n} (\hat{\mathbf{n}} \cdot \mathbf{B})\, \phi\, dA_n\right) + \int_{\partial A_n} (\phi \mathbf{E}) \cdot d\vec{\ell} - \int_{A_n} \hat{\mathbf{n}} \cdot [(\nabla\phi) \times \mathbf{E}]\, dA_n = 0. \tag{17}$$

The above-mentioned equation is the second master equation that stems from Faraday's law. (The **B** terms in the above equation indicate that these are the facial primal variables; the **E** terms are obtained at the edges of the mesh by application of a multidimensional Riemann solver; and the **E** terms are obtained within the faces of the grid cells by the application of a 1-D Riemann solver.)

As a side note, as for (12), (17) is true for any general manifold and even holds if the face/manifold that is integrated over is curved as long as $\hat{\mathbf{n}}$ is locally normal to the manifold and as long as the test function ϕ resides in that manifold. The formulation, therefore, applies naturally to elements with isoparametrically mapped curved surfaces. In other words, globally constraint-preserving DGTD schemes for CED on general curvilinear meshes are easily available.

Continuing with the case of $\hat{\mathbf{n}} = \hat{\mathbf{z}}$, the second term is an integral over the entire boundary of the z-face of the grid cell in Fig. 3(b). This integral picks up contributions from E_x and E_y at the boundary. These contributions are obtained from a one-dimensional Riemann solver. Note that the third term in (17) requires that the components of E_x and E_y at all locations on the z-face are known. In other words, even though (13) and the analogous equation in the y-direction only provide the components of the electric displacement at the boundaries, a strategy is needed for reconstructing the electric displacement vector field at all locations in the grid cell. In other words, it is apparent that a volumetric reconstruction strategy for the electric displacement vector field that is consistent with the boundary values in (13) and the analogous equation in the y-direction as well as the constraints in (1c) is an essential ingredient in any DG scheme for CED. Such second order, constraint-preserving reconstruction with nontrivial charge densities has been described in [28]. Also, Balsara *et al.* [29, Sec. III] reports higher order extensions of the same constraint-preserving reconstruction with nontrivial charge densities. The next few paragraphs will show how (17) is used to design a DG scheme at the second order.

Now let us be specific with respect to (17). On the bottom z-face of Fig. 3(b), the second-order accurate evolution of the z-component of the magnetic induction vector is asserted to be of the form

$$B^z(x,y,t) = B_0^z(t) + B_x^z(t)\left(\frac{x}{\Delta x}\right) + B_y^z(t)\left(\frac{y}{\Delta y}\right). \tag{18}$$

Note that suppressing the z-variation implies that both the bottom and top z-faces of Fig. 3(b) have the same z-component of the magnetic induction vector, thus ensuring that the constraint in (1d) is always satisfied for the magnetic induction.

The trial functions are $\phi(x,y) = 1$, $\phi(x,y) = (x/\Delta x)$ and $\phi(x,y) = (y/\Delta y)$. Using $\hat{\mathbf{n}} = \hat{\mathbf{z}}$ and the test function $\phi(x,y) = 1$ in (17) then yields

$$\frac{dB_0^z(t)}{dt} + \frac{1}{\Delta x}\begin{bmatrix} \left\langle E^{y^*}(x=\Delta x/2, y)\right\rangle_{\text{line avg}} \\ -\left\langle E^{y^*}(x=-\Delta x/2, y)\right\rangle_{\text{line avg}} \end{bmatrix} - \frac{1}{\Delta y}\begin{bmatrix} \left\langle E^{x^*}(x, y=\Delta y/2)\right\rangle_{\text{line avg}} \\ -\left\langle E^{x^*}(x, y=-\Delta y/2)\right\rangle_{\text{line avg}} \end{bmatrix} = 0. \tag{19}$$

Using $\hat{\mathbf{n}} = \hat{\mathbf{z}}$ and the test function $\phi(x,y) = (x/\Delta x)$ in (17) yields

$$\frac{1}{12}\frac{dB_x^z(t)}{dt} + \frac{1}{2\Delta x}\begin{bmatrix} \left\langle E^{y^*}(x=\Delta x/2, y)\right\rangle_{\text{line avg}} \\ +\left\langle E^{y^*}(x=-\Delta x/2, y)\right\rangle_{\text{line avg}} \end{bmatrix} - \frac{1}{\Delta y}\begin{bmatrix} \left\langle (x/\Delta x)\, E^{x^*}(x, y=\Delta y/2)\right\rangle_{\text{line avg}} \\ -\left\langle (x/\Delta x)\, E^{x^*}(x, y=-\Delta y/2)\right\rangle_{\text{line avg}} \end{bmatrix} - \frac{1}{\Delta x}\left\{E^y(x,y)\right\}_{\text{area avg}} = 0. \tag{20}$$

Using $\hat{\mathbf{n}} = \hat{\mathbf{z}}$ and the test function $\phi(x,y) = (y/\Delta y)$ in (17) further yields

$$\frac{1}{12}\frac{dB_y^z(t)}{dt} + \frac{1}{\Delta x}\begin{bmatrix} \left\langle (y/\Delta y)\, E^{y^*}(x=\Delta x/2, y)\right\rangle_{\text{line avg}} \\ -\left\langle (y/\Delta y)\, E^{y^*}(x=-\Delta x/2, y)\right\rangle_{\text{line avg}} \end{bmatrix} - \frac{1}{2\Delta y}\begin{bmatrix} \left\langle E^{x^*}(x, y=\Delta y/2)\right\rangle_{\text{line avg}} \\ +\left\langle E^{x^*}(x, y=-\Delta y/2)\right\rangle_{\text{line avg}} \end{bmatrix} + \frac{1}{\Delta y}\left\{E^x(x,y)\right\}_{\text{area avg}} = 0. \tag{21}$$

From the above-mentioned three equations, the angled brackets again represent suitably high-order line averages along the edges that surround the z-face. Note that the angled brackets in the above-mentioned three equations only contain the electric fields obtained from 1-D Riemann solvers. This is because the 2-D Riemann solver applied to the x-edges and y-edges of Fig. 3(b) reduces to a 1-D Riemann solver when the entire z-variation is suppressed. Also, note the introduction of curly brackets, i.e., $\{\}$, in (20) and (21). These curly brackets denote suitably high-order area averages within the z-face. As always, they must be obtained via a suitably high-order 2-D quadrature formula. Alternatively, since $E^x(x,y)$ and $E^y(x,y)$ are expressed in terms of an orthogonal basis set, the curly brackets may usually be evaluated analytically on a Cartesian mesh. Equations (20) and (21) indicate that the facial variation from (13) and the analogous equation in the y-direction should be used to obtain a second-order, constraint-preserving reconstruction within the element to obtain the electric fields $E^x(x, y)$ and $E^y(x, y)$. This completes the description of the second order, $\mathrm{P} = 1$, DGTD scheme for CED.

Note that (14) and the analogous equation in the y-direction ensure that the evolution of the electric displacement is constraint-preserving and follows the same Yee type update. As a result, a DGTD scheme for CED has been obtained that is the closest analogue of FDTD. The higher order modes, i.e., (15) and (16) for the displacement vector, do not contribute to the constraint-preservation as long as the mean flux contributed by those higher modes averages to zero.

Equations (19)–(21) indicate something else that is also very interesting. Observe that for a TE_z mode, that has been focused on here, the evolution equation for $B_z$reduces to a traditional conservation law. Applying traditional DG formulations to the evolution equation for B_z [i.e., to the last row of (2)] would also yield (19)–(21). This establishes a very nice consistency between the new DG-like schemes and traditional DG schemes. In the limit where both are expected to yield the same result, they indeed do yield the same result!

There is literature, though it is not usually accessed by the CED community, that shows that when constraints are ignored in the solution of a PDE, they produce spurious effects in the solution; see [55] and [56]. The previous references show this for MHD and general relativity; but the example in Section I drives home the point that the same is true for CED. The globally constraint-preserving DGTD method of this article will now be compared and contrasted to other variants of the DGTD method with vector fields [24]–[26]. The DGTD scheme in [24]–[26] is developed with curl-conforming basis functions for E and div-conforming basis functions for B. Because E is used as the primal variable, instead of D, the scheme would not precisely satisfy Gauss' law for the charge density, especially in regions of spatially-varying permittivity (though it may be possible to design the Hodge projection more carefully so that it does). Because in the scheme of this article the div-conforming reconstruction is used, for D and B, the exact satisfaction of both forms of Gauss' law is automatic. Besides, the basis functions of [24] reside in the volume of the element, whereas the basis functions in this work reside in the faces of each element. Because the basis functions here have simpler support, they are easier to extend to higher orders. The use of the multidimensional Riemann solver also helps to stabilize this article's DGTD scheme.

VI. Higher Order Time-Stepping Dissipation and Dispersion Properties of DGTD Schemes

There are two challenges in any time-stepping scheme for CED. First, the time-stepping should be high-order in time. Second, stiff source terms, which usually arise by way of large material conductivities, should be handled. To tackle the first challenge, FDTD uses not just a spatially staggered pair of meshes, but it also staggers the temporal update in time. As a result, in the first half-step, the **E** field contributes to the update of the **H** field; whereas, in the second half-step, the just-updated **H** field contributes to the update of the **E** field. This results in a leap-frog time-stepping that is only second-order accurate in time. Since leap-frog time-stepping is symplectic, FDTD conserves electromagnetic energy in a medium with constant material properties, though the same cannot be proven for a general medium. Despite that seeming advantage, the restriction of the time-stepping to second order also makes the FDTD scheme significantly dispersive. In general, a working application may trade spatial and temporal accuracies, with the result that temporal accuracy is usually desired in a numerical scheme that matches the spatial accuracy. Since the DGTD schemes described here have higher order extensions in space, they should be matched with similar higher order accuracies in time. In CED there may also be materials with large conductivities, which results in a PDE system with stiff source terms. To tackle this second challenge, and because of its very design, FDTD uses a half-implicit treatment of stiff source terms (think of large conductivities in metals). Since half-implicit methods are not very stable in the presence of very stiff source terms, i.e., in the presence of highly conductive metals, it may limit some FDTD applications.

Two well-known, modern, time-stepping strategies for PDEs show a pathway to higher order temporal accuracy whilst also providing for a more stable treatment of stiff source terms. The first strategy is based on Runge-Kutta time-stepping [57]–[62] with variants that handle stiff source terms in a fully implicit fashion being presented in [63] and [64]. Runge-Kutta schemes have a multi-stage structure, and each stage looks much like the other stage, which makes them easy to implement in code. Runge-Kutta time-stepping with better than fourth-order accurate time-stepping involves the use of additional intermediate stages to overcome the Butcher barriers; which makes these schemes inefficient at very high orders. Furthermore, the variants of Runge-Kutta schemes that can handle stiff source terms are limited to the third order of accuracy in the treatment of source terms. Runge-Kutta time-stepping that is adapted to CED with stiff source terms has been presented in [27]. For the sake of completeness, it must also be mentioned that exponential time differencing-based Runge-Kutta methods (known as ETDRK methods) have also been introduced [65]–[67] and those methods can go beyond third order, albeit with restrictions being placed on the structure of the source terms. For certain classes of CED problems, where the source terms are linear, but stiff, these ETDRK methods might prove adequate.

The second strategy, involving Arbitrary DERivatives in space and time (ADER) schemes offer a way out while overcoming the limitations of Runge-Kutta time-stepping. ADER schemes may be thought of as higher order extensions of Lax-Wendroff schemes; therefore, they offer the convenience of a single-stage time update. Early variants of ADER time-stepping [68]–[73], has found plenty of popular use. An accessible review of ADER schemes has been given in [74]. Such ADER schemes have been specialized for CED in [28] and [29] and they prove to be faster than Runge-Kutta schemes. ADER schemes may be extended to any order of accuracy in time and the fully implicit treatment of stiff source terms is equally accurate. When the ADER schemes are coupled to higher order FVTD or DGTD schemes, they also offer the advantage of the subcell resolution of variation in material properties. For situations where the two alternative time-stepping strategies are equally functional, they offer roughly similar dissipation and dispersion.

For CED simulations, propagation of numerical electromagnetic waves in a mesh with a minimum of dissipation and dispersion is desired. Here, it is very valuable to carry out a von Neumann stability analysis of globally constraint-preserving DGTD schemes where the spatial and temporal orders of accuracy are matched. Such a study is carried out in [31]. This article provides a considerable amount of detail and only a couple of illustrative examples are provided here.

In a von Neumann stability analysis, one starts with a time-harmonic plane wave and analyzes its dissipation and dispersion properties. Fig. 6 presents such a von Neumann stability analysis. Similar analyses have been carried out for FDTD in [3] and such analyses have provided very valuable insights into the fidelity with which FDTD propagates electromagnetic radiation. Fig. 6(a) from [31] shows the amplification factor for wave propagation in various directions relative to the mesh for waves that have a wavelength of five grid cells. Results are provided for the second-order P = 1 DGTD scheme, the third-order P = 2 DGTD scheme, the fourth-order P = 3 DGTD scheme and the Yee scheme. The temporal accuracy of the Runge-Kutta time-stepping matches the spatial accuracy of the DG scheme. Fig. 6(b) shows the phase velocity, normalized to unity, for the same four schemes.

Focusing first on Fig. 6(a), which pertains to dissipation, the second order, P = 1, DGTD scheme has an amplification factor that is smaller than unity by a substantial amount. As a result, it is rather dissipative when waves with a wavelength of five grid cells are represented on the computational mesh. The third-order, P = 2, DGTD scheme already shows a considerably reduced dissipation. The fourth-order, P = 3, DGTD scheme is almost free of dissipation and comparable to the Yee scheme, which is fully nondissipative on account of it being a symplectic scheme.

Focusing on Fig. 6(b), which pertains to dispersion, both the second-order, P = 1, DGTD scheme as well as the second-order Yee scheme are rather dispersive. By contrast, the third-order, P = 2, DGTD scheme exhibits substantially improved dispersion that lies much closer to the ideal value of unity for all directions of wave propagation. The fourth-order, P = 3, DGTD scheme shows an even more appealing result because the dispersion is practically perfect. Thus, with increasing order of accuracy, the DGTD schemes become closer to the ideal limit in their dissipation as well as their dispersion. Balsara and Käppeli [31, Tables III and IV] provide further quantitative detail about the dissipation and dispersion characteristics of the schemes shown here; and Table I of that article shows their limiting Courant numbers.

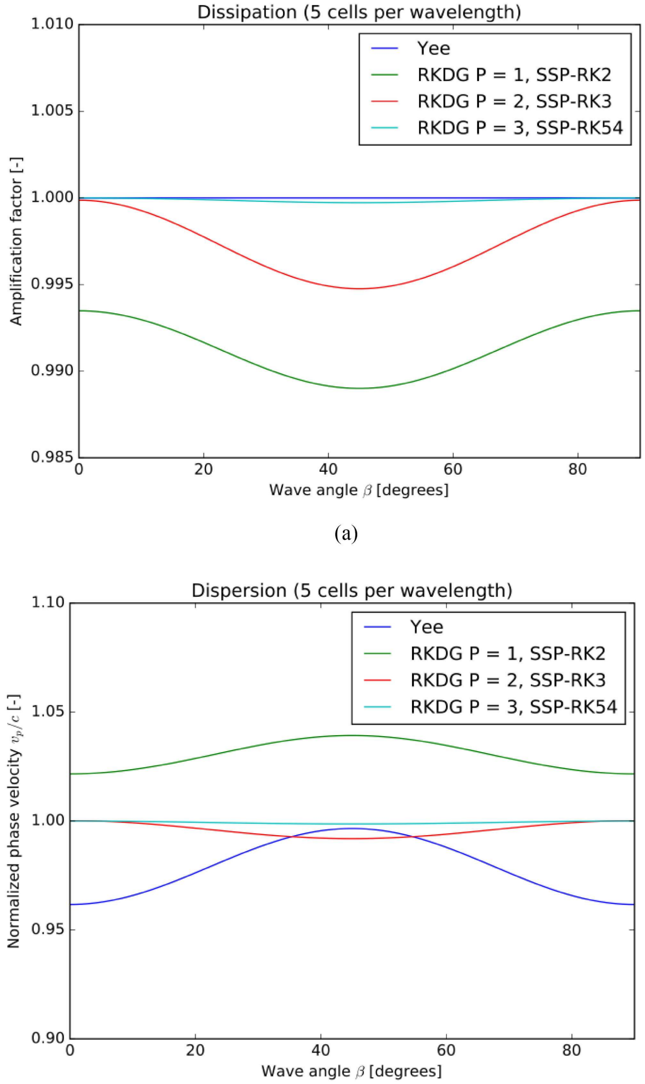

(a)

(b)

Fig. 6. (a) Amplification factor for wave propagation in various directions relative to the mesh for waves that have a wavelength of five grid cells. The green, red, cyan, and blue curves show the results for the second-order P = 1 DGTD scheme, the third-order P = 2 DGTD scheme, the fourth-order P = 3 DGTD scheme and the Yee scheme, respectively. The temporal accuracy matches the spatial accuracy of the scheme. (b) The phase velocity, normalized to unity, for the same four schemes using the same color coding. With increasing order of accuracy, the schemes become closer to the ideal limit. The results correspond to a CFL that is 95% of the maximum. "SSP-RK" in the legend stands for strong-stability preserving Runge-Kutta time-stepping. Figure courtesy of [31].

One of the vexing features of all DG schemes is that their limiting Courant number decreases with increasing order of accuracy. In [71], only the first few moments in a DG scheme are seen to yield a majority of the accuracy improvement. In other words, the higher moments may be reconstructed without any significant loss of accuracy. This gave rise to the nomenclature of a PNPM scheme. (PNPM schemes evolve an Nth order spatial polynomial, while spatially reconstructing higher order terms up to Mth order. For example, P0PM schemes yield the finite-volume class of schemes with Mth order of accuracy; while PMPM schemes are identical to DG schemes with Mth order of accuracy. For $0 < N < M$, new classes of schemes emerge.)

The major advantage of PNPM schemes is that their limiting CFL is usually identical to the limiting CFL of an Nth order scheme; therefore, with $N < M$ there is an improvement in the limiting CFL. The dispersion and dissipation characteristics of a PNPM scheme remain comparable to the corresponding characteristics of a PMPM scheme; yielding a very accurate family of schemes with improved CFL numbers compared to DG schemes. The result in [71] pertains to FV-based schemes for PDEs. An

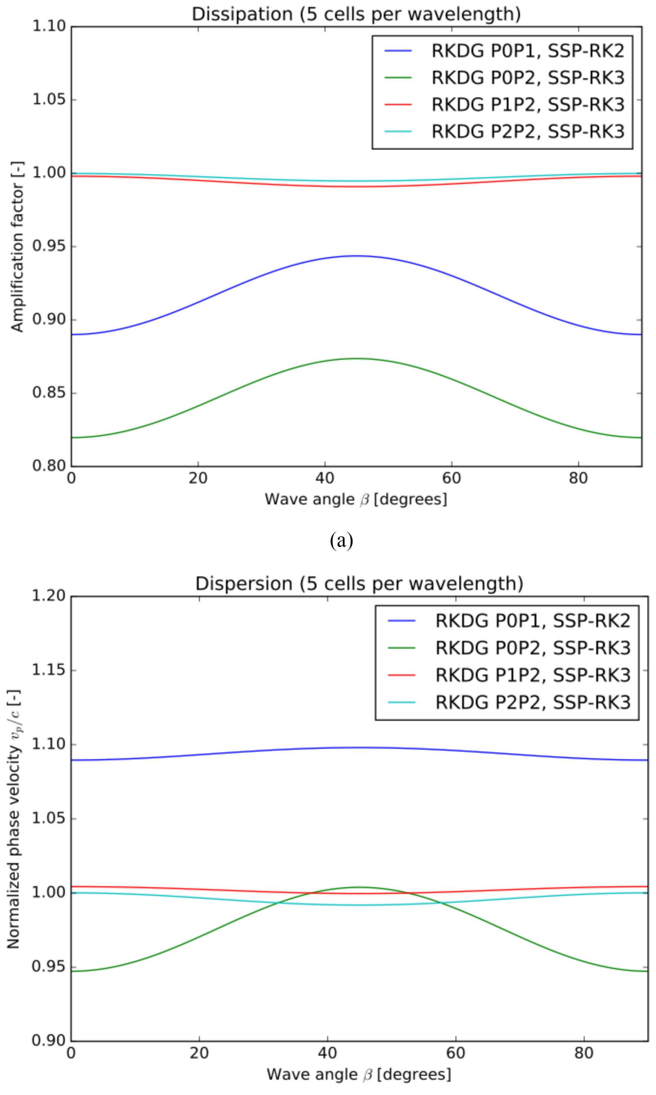

(a)

(b)

Fig. 7. Analogous to Fig. 6, except that it pertains to the wave propagation at various angles for POP1, POP2, P1P2, and P2P2 scheme for CED. The waves span five grid cells. The P2P2 scheme is just the P = 2 DGTD scheme and is shown for reference. The vertical scales in Fig. 7 are different from Fig. 6. (a) Amplification factor for wave propagation on various directions relative to the mesh for waves that have a wavelength of five grid cells. The blue, green, red, and cyan curves show the results for the second-order P0P1 scheme, the third-order P0P2 scheme, the third-order P1P2 scheme and the P2P2 schemes, respectively. (b) Phase velocity, normalized to unity, for the same four schemes using the same color coding. Figure courtesy of [31].

interesting question is, do the same twin advantages of large CFL without much degradation in dissipation and dispersion extend to constraint-preserving PNPM schemes? This question was answered in the affirmative in [31]. We provide details in the next paragraph.

Fig. 7 is analogous to Fig. 6, except that it pertains to the wave propagation at various angles for order P0P1, P0P2, P1P2, and P2P2 schemes for CED. The waves span five grid cells. The P2P2 scheme is just the P = 2 DGTD scheme and is shown for reference. The vertical scales in Fig. 7 are different from Fig. 6. The P0P1 and P0P2 schemes are second and third-order weighted essentially nonoscillatory schemes [43]–[45]. When the wavelength spans just five grid cells, there are deficiencies in these schemes because they try to reconstruct all the moments at each timestep. A comparison of the third-order P1P2 and P2P2 schemes shows a very interesting result. The P1P2 scheme provides almost the same high quality of wave propagation as the P2P2 scheme. This is because most of the variation within a grid cell is carried by the linear modes, which are indeed evolved consistently with the governing equations in the P1P2 scheme.

Consider the maximal CFL for both schemes when they are used along with a third order in time Runge-Kutta time-stepping strategy. Data for this case are available in [31, Tables I and II]. The P1P2 scheme sustains a maximal CFL of 0.3141, which is considerably larger than the maximal CFL of 0.1623 for the P2P2 scheme. Similar results have been reported for fourth-order accurate P1P3 schemes in [31], showing that a wealth of very favorable CED schemes exist that were hitherto fore unknown to the CED community!

In CED, there has been a substantial literature on time-stepping schemes that minimize dissipation and dispersion. Such attempts to obtain low dissipation and low dispersion schemes have indeed been presented within the context of Runge-Kutta time-stepping [75]–[78]. In a major recent breakthrough, Käppeli *et al.* [33], Chan and Tsai [79], and Grant *et al.* [80] realized that it is possible to not just evaluate the fluxes but also their time-derivatives. The article [33] is especially relevant because it is directly focused on DG schemes for CED. Balsara [49] shows that if the time-derivatives of the edge-centered update terms are also available then DG schemes for CED that minimize dissipation and dispersion whilst simultaneously permitting a larger CFL may be derived. The technology that makes this major advance possible is the invention of a multidimensional generalized Riemann problem solver by Balsara *et al.* [42]. This advance is pointed out as a way of illustrating to the interested reader that there is a considerable emergent up-side to the ideas described here.

VII. RESULTS

Several examples of the resolving abilities of FVTD and DGTD schemes have been documented in [28], [29], and [32]. Just a few results are highlighted here that emphasize the sub-cell resolving ability of these schemes. Because of space constraints, the problem setup is not described in this review paper because the problems have been documented thoroughly in the original literature.

The first example highlights the sub-cell resolution of the DGTD schemes presented here. Fig. 8, from [32], shows the interaction of an electromagnetic pulse that starts in air and interacts with a disk of radius 0.75 m having refractive index of 3. The disk is shown by the black circle. A Cartesian mesh was used even in the area spanned by the disk and no effort was made to conform the mesh to the disk boundary. This was a deliberate choice and is intended to show that our methods preserve their order property even when the problem geometry is not mapped to the mesh. Fig. 8(a)–(c) shows the z-component of the magnetic field at initial time, early time, and late time, respectively. The

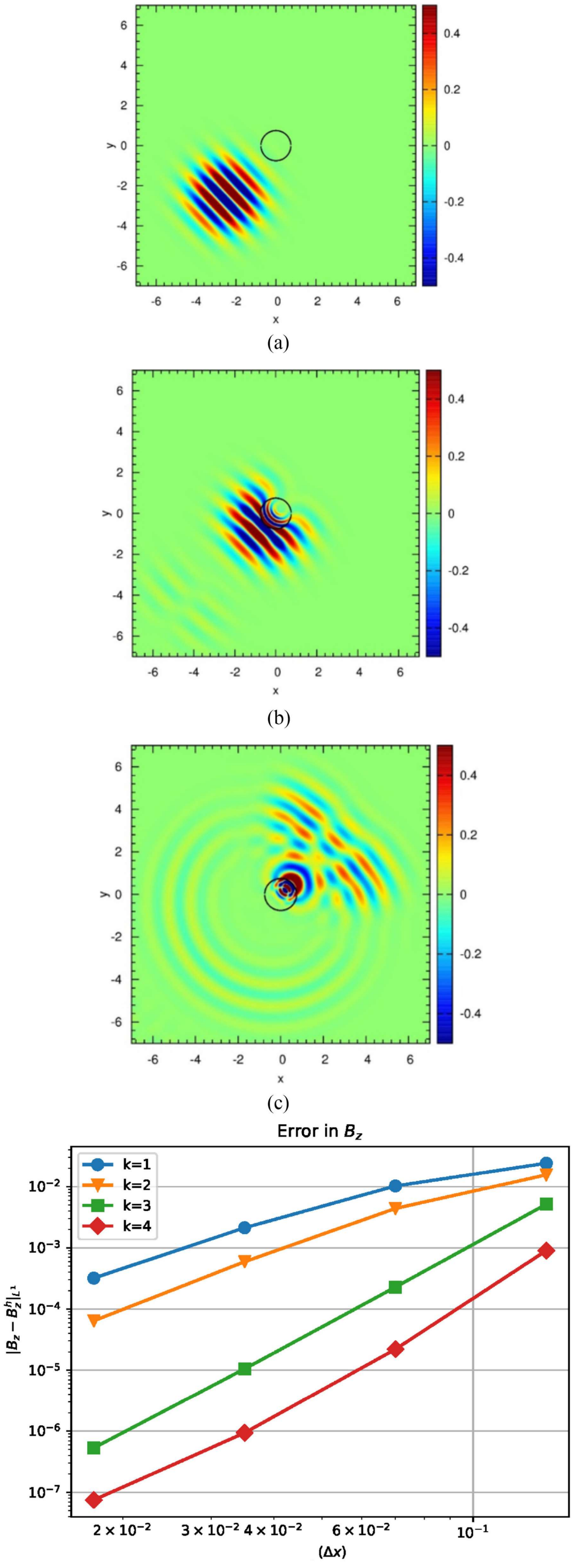

(a)

(b)

(c)

(d)

Fig. 8. Interaction of an electromagnetic pulse that starts in air and interacts with a disk having a refractive index of 3. The disk is shown by the black circle. (a)–(c) z-component of the magnetic field at initial time, early time, and late time, respectively. The x- and y-axes are in units of meters. (d) Error as a function of mesh size. Results are plotted for k varying from 1 to 4, where k refers to the degree of the 1-D polynomial used for reconstruction of the vector fields. Courtesy of [44].

radiation scatters off the disk and, because the disk and the wavelength of the radiation have comparable length scales, the scattering is substantial. Fig. 8(d) shows the error as a function of mesh size. The DGTD schemes meet their design accuracies despite the large variation in permittivity over just a few grid cells. From Fig. 8(d), the more accurate schemes are indeed more accurate even at the lowest resolutions. Moreover, as the mesh is refined, the more accurate schemes reach their design accuracies much faster. This highlights the subscale resolving abilities of the constraint-preserving DGTD schemes presented here.

The subscale resolving abilities of globally constraint-preserving DGTD schemes stem from multiple considerations. First, notice from the second terms in (12) and (17) that DG schemes have a very high-order accuracy treatment of the magnetic field and electric field along the edges of the mesh. This means that spatial variations along an edge may be picked up by these schemes. Second, notice from the third terms in (12) and (17) that DG schemes also have very high-order accuracy treatment of the magnetic field and electric field along the faces of the mesh. This means that the schemes can respond to even further spatial variations. Third, in addition to the spatial variation in electric and magnetic fields, the material properties are also reconstructed with the same order of accuracy as the underlying method. As a result, the entire spatial discretization can be responsive to subcell variations in the material properties. Fourth, the high-order temporal discretization afforded by ADER methods ensures that the full space-time dynamics respond to the spatial variation in material properties. For all these reasons, the FVTD and DGTD have excellent subcell resolution.

Section IV started by mentioning that with increasing order of accuracy, i.e., with the inclusion of higher moments, the DGTD schemes come increasingly close to having spectral accuracy (providing a "perfect" solution over the frequency range of interest). This is because all the higher moments are evolved in a fashion that is consistent with the governing equations, i.e., Maxwell's equations. However, in order for this accuracy to be closest to its optimum, the moments should evolve entirely consistently with the governing equations and should not be interfered with in the course of a time step because of any other considerations. For CFD applications, the presence of shocks forces one to interfere with the higher moments using a process called nonlinear limiting. This degrades the accuracy of CFD applications that rely on DG methods. For CED applications, the waves are sufficiently smooth on the mesh with the result that this process of nonlinear limiting seems to be unnecessary even when there are substantial spatial variations in permittivity and permeability. For example, all the tests shown in Fig. 8 were carried out *without* the application of a limiter. This has the happy consequence that CED applications may indeed achieve the full subcell resolving potential of the underlying DGTD schemes presented here.

FDTD was shown to use symplectic time-integration, which ensures energy conservation at least in media with uniform permittivity and permeability. Fig. 7(a) shows that FDTD is, therefore, free of dissipation. However, Fig. 7(b) shows the disadvantage of a second-order accurate, leap-frog based time-integration, namely appreciable numerical dispersion, especially yielding numerical velocity anisotropy. In other words, the electromagnetic energy is conserved, however, there is no control over the speed with which it propagates on the computational mesh. Moreover, the propagation is very anisotropic; which may be worrisome. The higher order time-integration strategies, especially when they are conjoined to higher order spatial reconstruction, are intended to fix those problems. This is easily apparent in the nearly dissipation-free and dispersion-free properties of the fourth-order DGTD scheme shown in Fig. 7(a) and (b). However, it is desirable to demonstrate energy conservation on a practical problem, especially one where material properties vary widely over space.

Fig. 9, from [32], shows the evolution of electromagnetic energy as a function of time for the compact Gaussian pulse that is incident on a refractive disk from Fig. 8. Globally constraint-preserving DGTD schemes were used. Fig. 9(a) shows the evolution of total energy as a function of time for a 100×100 grid cell simulation at second (blue curve), third (orange curve), fourth (green curve), and fifth (red curve) orders of accuracy. At those very low resolutions, only the fifth-order scheme comes close to conserving electromagnetic energy. Fig. 9(b) shows the same for a 200 × 200 grid-cell simulation; and at that resolution, the fourth-order scheme has almost caught up with the fifth-order scheme. Fig. 9(c) shows the same for a 400 × 400 grid-cell simulation; and at this resolution, the fourth- and fifth-order schemes are practically perfectly energy conserving. Fig. 9(d) shows the same for an 800 × 800 grid-cell simulation, at which the third-order scheme has also started catching up with the fourth- and fifth-order schemes.

Therefore, higher order constraint-preserving DGTD schemes are very proficient at conserving electromagnetic energy on meshes with modest resolutions even when there are subscale variations in the material properties. Moreover, combining the results from Figs. 6 and 9, this is accomplished with minimal dissipation and dispersion.

For engineering problems, it is also important to show that the numerical modeling methods are cost-effective. In other words, a higher order scheme would indeed cost more per timestep than a lower order scheme because it evolves more variables in order to retain its higher accuracy. However, it should provide some improved advantages. The previous paragraph documented those advantages in terms of low dissipation and dispersion and conservation of electromagnetic energy. The next paragraph documents the advantages in terms of the time to solution.

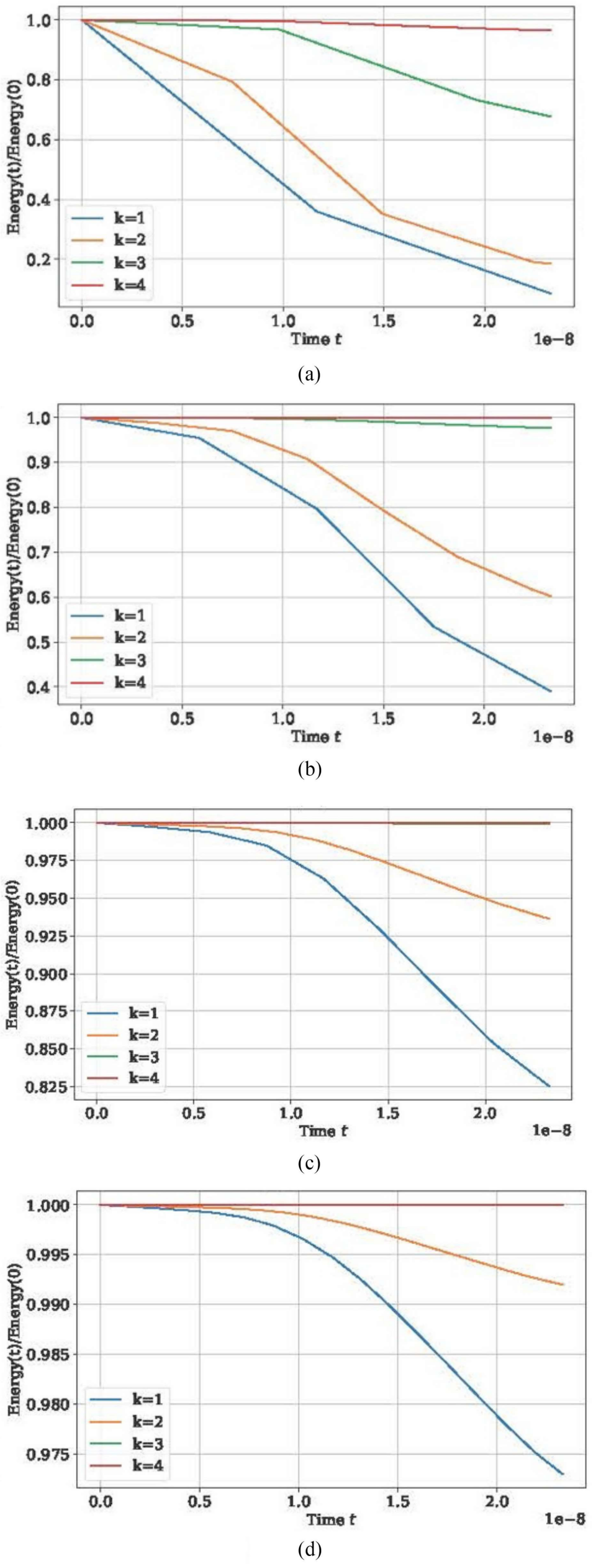

(a)

(b)

(c)

(d)

Fig. 9. Evolution of electromagnetic energy as a function of time for the compact Gaussian pulse that is incident on a refractive disk as seen in Fig. 8. (a) Evolution of total energy as a function of time for a 100 × 100 grid-cell simulation at second (blue curve), third (orange curve), fourth (green curve), and fifth (red curve) orders of accuracy (*k* refers to the degree of the 1-D polynomial used for reconstruction of the vector fields). (b) Same for a 200 × 200 grid-cell simulation. (c) Same for a 400 × 400 grid-cell simulation. (d) Same for an 800 × 800 grid-cell simulation. Courtesy of [44].

Fig. 10, from [32], shows the Log of the error versus the Log of the relative time to solution for the second-, third-, fourth- and fifth-order DGTD-based CED schemes. The figure documents data for the compact Gaussian pulse incident upon the refractive disk from Fig. 8. If low accuracies are acceptable, the second-order (blue) or third-order (orange) order schemes are optimal. However, if high accuracies are desired, the fourth- and fifth-order schemes (green and red) obtain the most accurate solution in the least possible time. Extrapolation of the blue and orange curves in Fig. 10 clearly shows that if the highest orders of

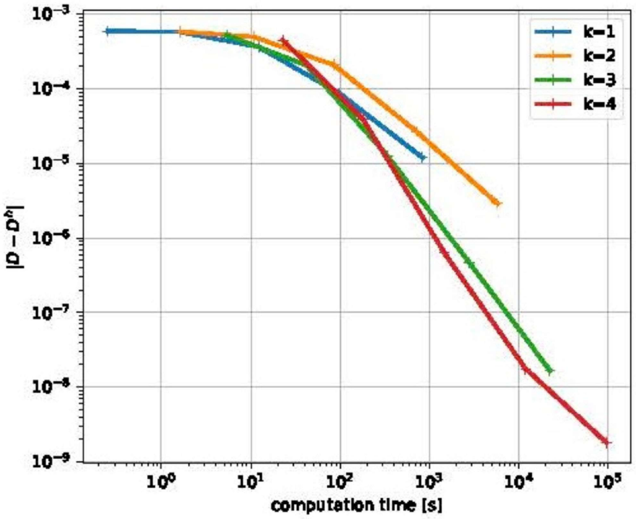

Fig. 10. Log of the error versus the Log of the relative time to solution for the second-, third-, fourth-, and fifth-order DGTD-based CED schemes for the case of a compact Gaussian pulse that is incident on a refractive disk from Fig. 8. Courtesy of [32].

accuracy are desired, the lower order schemes would take two or more orders of magnitude more time to the solution than the higher order schemes! This discussion shows that the higher order FVTD and DGTD schemes presented here may indeed justify their higher cost by offering a highly accurate solution at the lowest possible computational cost.

The beginning of Section V mentioned that any time-stepping scheme for CED presents two challenges. The first challenge consists of retaining temporal accuracy that matches the spatial accuracy, and that has been addressed in the preceding paragraphs of this section. However, the second challenge consists of the treatment of stiff source terms. On this front, the ADER time-stepping, with its very natural incorporation of fully implicitly-treated stiff source terms, shows its strengths. This is addressed next.

Suppose the skin depth in a conductor needs to be resolved. Some materials, like carbon and copper, have enormously large conductivities. Therefore, one has to use ADER methods that are fully implicit in their treatment of the conductivity whilst also retaining the advantages of high-order of accuracy. Using an example for electromagnetic wave propagation in carbon and copper developed in [28] and [29] numerical results that accurately match the analytic results will be shown, even when the skin depth is resolved with no more than ten grid cells. A fourth-order-accurate ADER-FVTD scheme is used. Fig. 11(a) and (b) shows the variations of B_z with radial distance inside carbon and copper, respectively. The exponentially decaying envelopes are also over-plotted. Fig. 11(c) and (d) presents the structure of the numerical envelopes (red crosses) and the analytical envelopes (blue curve) on a semi-log scale for carbon and copper, respectively. The numerically obtained envelopes match extraordinarily well with the analytical envelopes.

Just as with the problem of a Gaussian pulse interacting with a dielectric disk in Fig. 8, the new higher order methods offer

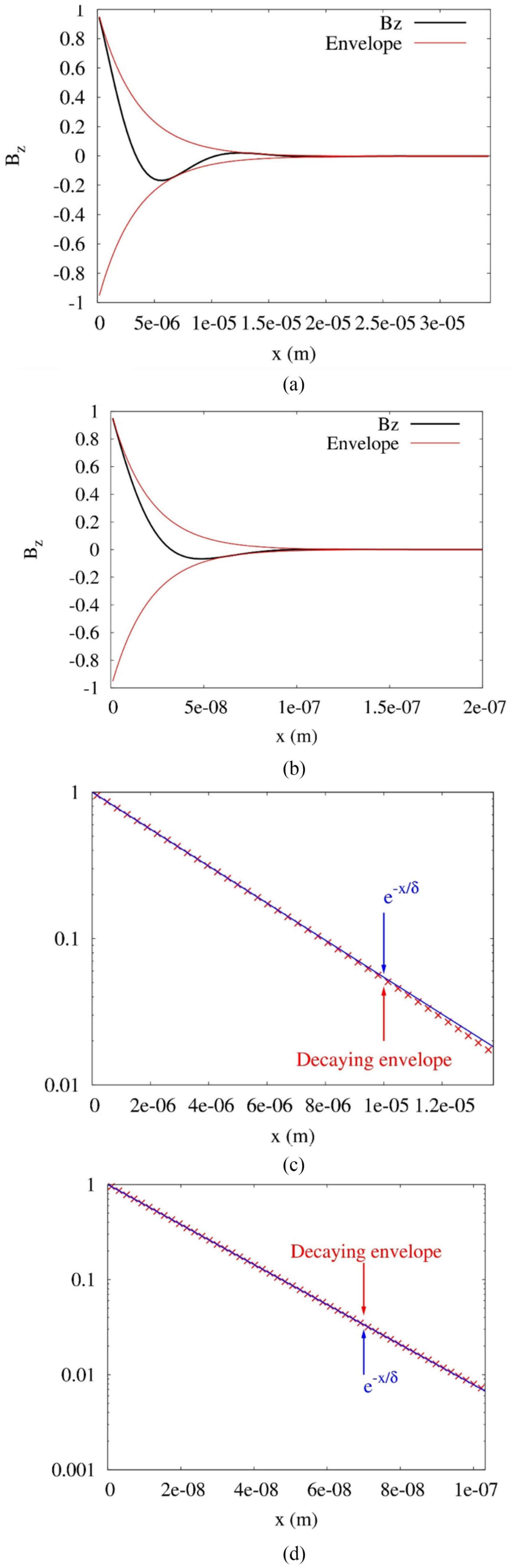

Fig. 11. (a) and (b) Radial variations of B_z (black lines) and the decaying envelopes (red lines) inside carbon and copper, respectively. (c) and (d) Structure of the numerically obtained envelopes (red crosses) and the analytical envelopes (blue curve) on a semi-log scale for carbon and copper, respectively. For carbon, the plane wave has a wavelength of 1.38×10^{-5} inside the material. For copper, the plane wave has a wavelength of 1.3×10^{-7} inside the material. Courtesy of [29].

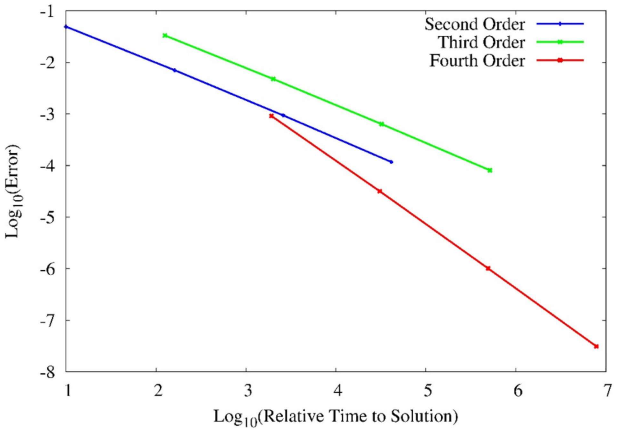

Fig. 12. Log of the error versus the Log of the relative time to solution for the second-, third-, and fourth-order ADER-FVTD-based CED schemes for the case of decaying propagation of the electromagnetic wave in copper from Fig. 11(b). Courtesy of [28], [29].

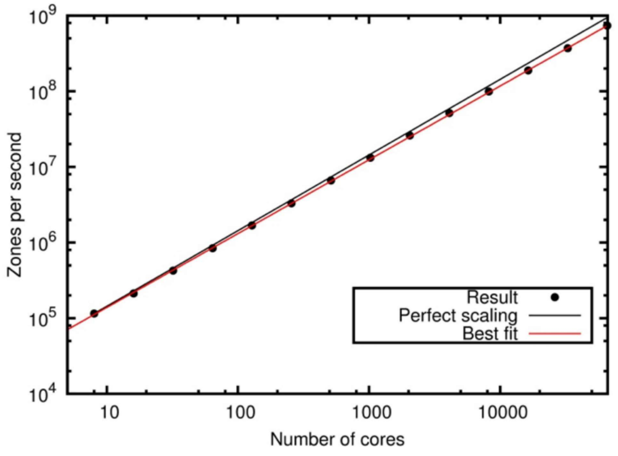

Fig. 13. Weak scaling study using the RIEMANN code on NCSA's Blue Waters supercomputer. The dots show data points. The black line shows an ideal speedup. The red line is a best fit for our data. The code scales with almost perfect scalability. Courtesy of [81].

lowest time-to-solution for a desired level of accuracy even in the presence of extremely stiff source terms. Fig. 12, from [28] and [29], show the Log of the error versus the Log of the relative time to solution for the second-, third-, and fourth-order ADER-FVTD-based CED schemes. This figure documents data for the decaying propagation of electromagnetic waves in copper from Fig. 11(b). If low accuracies are acceptable, the second-order (blue) or third-order (green) schemes are optimal. However, if high accuracies are desired, the fourth-order scheme (red) obtains the most accurate solution in the least possible time. In this problem, the ADER time-stepping, with its very high-order accurate and very stable treatment of stiff source terms, indeed shows its strengths.

Finally, it is useful to show that the methods presented here are extremely scalable. This is very timely, as PetaScale supercomputers have become relatively common, and the scientific community is gearing up for the advent of ExaScale supercomputers. Fig. 13 shows a weak scaling study using the first author's *RIEMANN* code from [81] on NCSA's Blue Waters system. The dots show data points. The black line shows an ideal speedup. The red line is a best fit to our data. The code scales with almost perfect scalability. While the results shown are for a constraint-preserving MHD code, it shares all the same algorithmic and data structures as a constraint-preserving CED code. As a result, the CED algorithms presented in this article are expected to have similar scalability.

VIII. CONCLUSION

In this article, which is partially a novel synthesis and partially a review, a synoptic view of the state of the art in emerging high order FVTD and DGTD methods was provided. These methods were invented by the first author within the context of numerical MHD, which shares the same Yee-type mesh structure as FDTD schemes for CED. The methods were intended to be the closest cousins of FDTD methods, in that they preserved all the same global constraints that are intrinsic to FDTD. The synthesis presented here was absolutely novel and had never before been affected.

The major building blocks that go into these methods were reviewed. The reader has also been pointed to the original source literature where the first author invented a majority of these methods. New perspectives were presented on the material that was reviewed here, so that even those who know the literature may never have seen it presented from the present perspective.

The first major building block consisted of constraint-preserving reconstruction. This ensures that the scheme starts with facial primal fields, just as in FDTD. However, in globally constraint-preserving FVTD and DGTD methods, the same control volume was used instead of the pair of staggered control volumes in FDTD. The use of facial primal fields naturally leads to the same Yee-type arrangement of variables that was used in FDTD; although the collocation of primal variables was different. However, now a high-order constraint-preserving reconstruction was used so that the entire vector fields for electric displacement and magnetic induction were reconstructed over the entire volume of the mesh. This was a crucial step for going to higher orders because it ensured that the entire governing equations were applicable at all locations of the computational mesh. Further, these advances were applicable to both structured and unstructured meshes, including curvilinear meshes that may be isoparametrically mapped. This extends the geometric flexibility of the methods presented here.

Once the constraint-preserving vector fields for electric displacement and magnetic induction were available at all locations on the mesh, the electric field and magnetic field at the grid cell edges are needed. This was completed with the help of a multidimensional Riemann solver. The intuitive ideas behind the multidimensional Riemann solver were explained in some detail, and further pointers to the original literature were given. As before, the multidimensional Riemann solver technology may be extended to structured and unstructured meshes, including meshes with curved boundaries. This extends the geometric flexibility of the methods presented here.

The globally constraint-preserving DGTD method was described in some detail. This included a fundamental paradigm shift in the development of DG methods. While previous DG methods were based on applying identities involving Gauss' law in weak form to the volumetric elements of a mesh, the newer methods were based on applying identities involving Stokes' law in weak form to the facial elements of the mesh. This fundamental paradigm shift was crucial for obtaining the globally constraint-preserving DGTD methods in this article. Moreover, the lowest-order terms in the DGTD methods followed the same style of constraint-preserving update that was present in FDTD. Thus a strong connection between the globally constraint-preserving DGTD methods and the original FDTD was established. Pointers to the original literature were also provided.

Time-stepping schemes were then discussed including ADER schemes and other modern schemes. By matching the order of accuracy in the spatial and temporal updates, very high-order space-time methods were shown for CED. The higher order methods in this family of methods were shown to be especially proficient at minimizing, even virtually eliminating, numerical dispersion, and dissipation errors while conserving electromagnetic energy.

With the help of a couple of rigorous problems, the new globally constraint-preserving FVTD and DGTD methods were shown to meet their design accuracies. The subcell resolving abilities of the higher order DGTD methods were documented in considerable detail. The higher order methods were also demonstrated to offer the shortest time to solution, especially when very high accuracies are demanded. The exceptional scalability of these methods on modern-day supercomputers was also documented.

ACKNOWLEDGMENT

Several simulations were performed on a cluster at the University of Notre Dame that is run by the Center for Research Computing. Computer support on NSF's XSEDE and Blue Waters computing resources is also acknowledged.

REFERENCES

[1] K. S. Yee, "Numerical solution of initial boundary value problems involving Maxwell equation in an isotropic media," *IEEE Trans. Antenna Propag.*, vol. AP-14, no. 3, pp. 302–307, 1966.

[2] A. Taflove, "Review of the formulation and applications of the finite-difference time-domain method for numerical modeling of electromagnetic wave interactions with arbitrary structures," *Wave Motion*, vol. 10, pp. 547–582, 1988.

[3] A. Taflove and S. Hagness, in *Computational Electrodynamics: The Finite-Difference Time-Domain Method*, 3rd ed. Norwood, MA, USA: Artech House, 2005.

[4] A. Taflove and S. Hagness, in *Finite Difference Time Domain Solution of Maxwell's Equations*. Hoboken, NJ, USA: Wiley, 2016, pp. 1–33.

[5] A. Taflove, A. Oskooi, and S. Johnson, in *Advances in FDTD Computational Electrodynamics – Photonics and Nanotechnology*. Norwood, MA, USA: Artech House, 2013.

[6] C.-D. Munz, P. Omnes, R. Schneider, E. Sonnendrücker, and U. Voß, "Divergence correction techniques for Maxwell solvers based on a hyperbolic model," *J. Comput. Phys.*, vol. 161, pp. 484–511, 2000.

[7] T. Z. Ismagilov, "Second order finite volume scheme for Maxwell's equations with discontinuous electromagnetic properties on unstructured meshes," *J. Comput. Phys.*, vol. 282, pp. 33–42, 2015.

[8] A. Barbas and P. Velarde, "Development of a Godunov method for Maxwell's equations with Adaptive Mesh Refinement," *J. Comput. Phys.*, vol. 300, pp. 186–201, 2016.

[9] W. H. Reed and T. R. Hill, "Triangular mesh methods for the neutron transport equation," Technical Report LA-UR-73-479, Los Alamos Sci. Lab., Los Alamos, NM, USA, 1973.

[10] B. Cockburn and C.-W. Shu, "TVB Runge-Kutta local projection discontinuous Galerkin finite element method for conservation laws II: General framework," *Math. Comput.*, vol. 52, pp. 411–435, 1989.

[11] B. Cockburn and C.-W. Shu, "The Runge-Kutta discontinuous Galerkin method for conservation laws V: Multidimensional systems," *J. Comput. Phys.*, vol. 141, pp. 199–224, 1998.

[12] B. Cockburn and C.-W. Shu, "Runge-Kutta Discontinuous Galerkin methods for convection dominated problems," *J. Sci. Comput.*, vol. 16, pp. 173–261, 2001.

[13] B. Cockburn, S. Hou, and C.-W. Shu, "TVB Runge-Kutta local projection discontinuous Galerkin finite element method for conservation laws IV: The multidimensional case," *J. Comput. Phys.*, vol. 54, pp. 545–581, 1990.

[14] J. S. Hesthaven and T. Warburton, "Nodal high-order methods on unstructured grids: I. Time-domain solution of Maxwell's equations," *J. Comput. Phys.*, vol. 181, pp. 186–221, 2002.

[15] B. Cockburn, F. Li, and C.-W. Shu, "Locally discontinuous Galerkin methods for the Maxwell equations," *J. Comput. Phys.*, vol. 194, pp. 588–610, 2004.

[16] F. Kretzschmar, S. M. Schnepp, I. Tsukerman, and T. Weiland, "Discontinuous Galerkin methods with Trefftz approximations," *J. Comput. Appl. Math.*, vol. 270, pp. 211–222, 2014.

[17] H. Egger, F. Kretzschmar, S. M. Schnepp, I. Tsukerman, and T. Weiland, "Transparent boundary conditions for a discontinuous Galerkin Trefftz method," *Appl. Math. Comput.*, vol. 267, pp. 42–55, 2015.

[18] V. Bokil, Y. Chang, Y. Jiang, and F. Li, "Energy stable discontinuous Galerkin methods for Maxwell's equations in nonlinear optical media," *J. Comput. Phys.*, vol. 350, pp. 420–452, 2017.

[19] J. Chen and Q. H. Liu, "Discontinuous Galerkin time-domain methods for multiscale electromagnetic simulations: A review," *Proc. IEEE*, vol. 101, no. 2, pp. 242–254, Feb. 2013.

[20] Q. Ren, Q. Sun, L. Tobón, Q. Zhan, and Q. H. Liu, "EB scheme-based hybrid SE-FE DGTD method for multiscale EM simulations," *IEEE Trans. Antennas Propag.*, vol. 64, no. 9, pp. 4088–4091, Sep. 2016.

[21] H. Wang, L. Xu, B. Li, S. Descombes, and S. Lantéri, "A new family of exponential-based high-order DGTD methods for modeling 3-D transient multiscale electromagnetic problems," *IEEE Trans. Antennas Propag.*, vol. 65, no. 11, pp. 5960–5974, Nov. 2017.

[22] Q. Sun, R. Zhang, Q. Zhan, and Q.H. Liu, "A novel coupling algorithm for perfectly matched layer with wave equation-based discontinuous Galerkin time-domain method," *IEEE Trans. Antennas Propag.*, vol. 66, no. 1, pp. 255–261, Jan. 2018.

[23] L. D. Angulo, J. Alvarez, M. F. Pantoja, S. G. Garcia, and A. R. Bretones, "Discontinuous Galerkin time domain methods in computational electrodynamics: State of the art," *Forum Electromagn. Res. Methods Appl. Technol.*, vol. 10, pp. 1–24, 2015.

[24] L. E. Tobon, Q. Ren, and Q. H. Liu, "A new efficient 3D discontinuous Galerkin time domain (DGTD) method for large and multiscale electromagnetic simulations," *J. Comput. Phys.*, vol. 283, pp. 374–387, 2015.

[25] Q. Sun, Q. Ren, Q. Zhan, and Q. H. Liu, "3-D domain decomposition based hybrid finite-difference time-domain/finite-element time-domain method with non-conformal meshes," *IEEE Trans. Microw. Theory Techn.*, vol. 65, no. 10, pp. 3682–3688, Oct. 2017.

[26] Q. Sun, R. Zhang, Q. Zhan, and Q. H. Liu, "3-D implicit-explicit hybrid finite difference/spectral element/finite element time domain method without a buffer zone," *IEEE Trans. Antennas Propag.*, vol. 67, no. 8, pp. 5469–5476, Aug. 2019.

[27] D. S. Balsara, T. Amano, S. Garain, and J. Kim, "High order accuracy divergence-free scheme for the electrodynamics of relativistic plasmas with multidimensional Riemann solvers," *J. Comput. Phys.*, vol. 318, pp. 169–200, 2016.

[28] D. S. Balsara, A. Taflove, S. Garain, and G. Montecinos, "Computational electrodynamics in material media with constraint-preservation, multidimensional riemann solvers and sub-cell resolution – Part I, second-order FVTD schemes," *J. Comput. Phys.*, vol. 349, pp. 604–635, 2017.

[29] D. S. Balsara, A. Taflove, S. Garain, and G. Montecinos, "Computational electrodynamics in material media with constraint-preservation, multidimensional riemann solvers and sub-cell resolution – Part II, higher-order FVTD schemes," *J. Comput. Phys.*, vol. 354, pp. 613–645, 2018.

[30] D. S. Balsara, A. Hazra, S. Garain, and P. Chandrashekar, "Multidimensional generalized Riemann problem solver for Maxwell's equations," *J. Comput. Phys.*, 2019.

[31] D. S. Balsara and R. Käppeli, "von Neumann stability analysis of globally constraint-preserving DGTD and PNPM schemes for the Maxwell equations using multidimensional Riemann solvers," *J. Comput. Phys.*, vol. 376, pp. 1108–1137, 2019.

[32] A. Hazra, P. Chandrashekar, and D. S. Balsara, "Globally constraint-preserving FR/DG scheme for Maxwell's equations at all orders," *J. Comput. Phys.*, vol. 394, pp. 298–328, 2019.

[33] R. Käppeli, D. S. Balsara, P. Chandrashekar, and A. Hazra, "Globally constraint-preserving, DG(TD)2 schemes for computational electrodynamics based on two-derivative Runge-Kutta timestepping and multidimensional generalized Riemann problem solvers – A von Neumann stability analysis," *J. Comput. Phys.*, to be published.

[34] D. S. Balsara and D. S. Spicer, "A staggered mesh algorithm using high order Godunov fluxes to ensure solenoidal magnetic fields in magnetohydrodynamic simulations," *J. Comput. Phys.*, vol. 149, pp. 270–292, 1999.

[35] D. S. Balsara and R. Käppeli, "von Neumann stability analysis of globally divergence-free RKDG and PNPM schemes for the induction equation using multidimensional Riemann solvers," *J. Comput. Phys.*, vol. 336, pp. 104–127, 2017.

[36] D. S. Balsara, R. Kumar, and P. Chandrashekar, "Globally divergence-free DG scheme for ideal compressible MHD," *J. Comput. Phys.*, 2019.

[37] D. S. Balsara, "Divergence-free adaptive mesh refinement for magnetohydrodynamics," *J. Comput. Phys.*, vol. 174, pp. 614–648, 2001.

[38] D. S. Balsara, "Second-order-accurate schemes for magnetohydrodynamics with divergence-free reconstruction," *Astrophys. J. Suppl.*, vol. 151, pp. 149–184, 2004.

[39] D. S. Balsara, "Divergence-free reconstruction of magnetic fields and WENO schemes for magnetohydrodynamics," *J. Comput. Phys.*, vol. 228, pp. 5040–5056, 2009.

[40] D. S. Balsara and M. Dumbser, "Divergence-free MHD on unstructured meshes using high order finite volume schemes based on multidimensional Riemann solvers," *J. Comput. Phys.*, vol. 299, pp. 687–715, 2015.

[41] Z. Xu, D. S. Balsara, and H. Du, "Divergence-free WENO reconstruction-based finite volume scheme for ideal MHD equations on triangular meshes," *Commun. Comput. Phys.*, vol. 19, no. 04, pp. 841–880, 2016.

[42] D. S. Balsara, V. Florinski, S. Garain, S. Subramanyan, and K. F. Gurski, "Efficient, divergence-free high order MHD on 3D spherical meshes with optimal geodesic mapping," *Monthly Notices Roy. Astron. Soc.*, vol. 487, pp. 1283–1314, 2019.

[43] G.-S. Jiang and C.-W. Shu, "Efficient implementation of weighted ENO schemes," *J. Comput. Phys.*, vol. 126, pp. 202–228, 1996.

[44] D. S. Balsara and C.-W. Shu, "Monotonicity preserving weighted non-oscillatory schemes with increasingly high order of accuracy," *J. Comput. Phys.*, vol. 160, pp. 405–452, 2000.

[45] D. S. Balsara, S. Garain, and C.-W. Shu, "An efficient class of WENO schemes with adaptive order," *J. Comput. Phys.*, vol. 326, pp. 780–804, 2016.

[46] C. W. Schulz-Rinne, J. P. Collins, and H. M. Glaz, "Numerical solution of the Riemann problem for two-dimensional gas dynamics," *SIAM J. Sci. Comput.*, vol. 14, no. 7, pp. 1394–1414, 1993.

[47] D. S. Balsara, "Multidimensional HLLE Riemann solver; application to Euler and magnetohydrodynamic flows," *J. Comput. Phys.*, vol. 229, pp. 1970–1993, 2010.

[48] D. S. Balsara, "A two-dimensional HLLC Riemann solver for conservation laws: Application to Euler and magnetohydrodynamic flows," *J. Comput. Phys.*, vol. 231, pp. 7476–7503, 2012.

[49] D. S. Balsara, "Multidimensional Riemann problem with self-similar internal structure – Part I – Application to hyperbolic conservation laws on structured meshes," *J. Comput. Phys.*, vol. 277, pp. 163–200, 2014.

[50] D. S. Balsara, "Three dimensional HLL Riemann solver for structured meshes; application to Euler and MHD flow," *J. Comput. Phys.*, vol. 295, pp. 1–23, 2015.

[51] D. S. Balsara, M. Dumbser, and R. Abgrall, "Multidimensional HLL and HLLC Riemann solvers for unstructured meshes – With application to Euler and MHD flows," *J. Comput. Phys.*, vol. 261, pp. 172–208, 2014.

[52] D. S. Balsara and M. Dumbser, "Multidimensional Riemann problem with self-similar internal structure – Part II – Application to hyperbolic conservation laws on unstructured meshes," *J. Comput. Phys.*, vol. 287, pp. 269–292, 2015.

[53] D. S. Balsara *et al.*, "A two-dimensional Riemann solver with self-similar sub-structure – Alternative formulation based on least squares projection," *J. Comput. Phys.*, vol. 304, pp. 138–161, 2016.

[54] D. S. Balsara and B. Nkonga, "Formulating multidimensional Riemann solvers in similarity variables – Part III: A multidimensional analogue of the HLLI Riemann solver for conservative hyperbolic systems," *J. Comput. Phys.*, vol. 346, pp. 25–48, 2017.

[55] D. S. Balsara and J. S. Kim, "An intercomparison between divergence-cleaning and staggered mesh formulations for numerical magnetohydrodynamics," *Astrophys. J.*, vol. 602, pp. 1079–1090, 2004.

[56] M. Dumbser, F. Fambri, E. Gaburro, and E. Reinarz, "On GLM curl cleaning for a first order reduction of the CCZ4 formulation of the Einstein field equations," *J. Comput. Phys.*, vol. 404, 2020, Art no. 109088.

[57] C.-W. Shu and S.J. Osher, "Efficient implementation of essentially non-oscillatory shock capturing schemes," *J. Comput. Phys.*, vol. 77, pp. 439–471, 1988.

[58] C.-W. Shu and S. J. Osher, "Efficient implementation of essentially non-oscillatory shock capturing schemes II," *J. Comput. Phys.*, vol. 83, pp. 32–78, 1989.

[59] C.-W. Shu, "Total variation-diminishing time discretizations," *SIAM J. Sci. Stat. Comput.*, vol. 9, pp. 1073–1084, 1988.

[60] R. J. Spiteri and S. J. Ruuth, "A new class of optimal high-order strong-stability-preserving time-stepping schemes," *SIAM J. Numer. Anal.*, vol. 40, pp. 469–491, 2002.

[61] R. J. Spiteri and S. J. Ruuth, "Non-linear evolution using optimal fourth-order strong-stability-preserving Runge-Kutta methods," *Math. Comput. Simul.*, vol. 62, pp. 125–135, 2003.

[62] S. Gottlieb, C.-W. Shu, and E. Tadmor, "Strong stability-preserving higher order time discretization methods," *SIAM Rev.*, vol. 43, no. 1, pp. 89–112, 2001.

[63] L. Pareschi and G. Russo, "Implicit-explicit Runge-Kutta schemes and applications to hyperbolic systems with relaxation," *J. Sci. Comput.*, vol. 25, pp. 129–155, 2005.

[64] F. Kupka, N. Happenhofer, I. Higueras, and O. Koch, "Total-variation-diminishing implicit–explicit Runge–Kutta methods for the simulation of double-diffusive convection in astrophysics," *J. Comput. Phys.*, vol. 231, pp. 3561–3586, 2012.

[65] B. L. Ehle, "A-stable methods and Padé approximations to the exponential," *SIAM J. Math. Anal.*, vol. 4, pp. 671–680, 1973.

[66] S. M. Cox and P. C. Matthews, "Exponential time differencing for stiff systems," *J. Comput. Phys.*, vol. 176, pp. 430–455, 2002.

[67] D. S. Balsara, J. Li, and G. Montecinos, "An efficient, second order accurate, universal generalized Riemann problem solver based on the HLLI Riemann solver," *J. Comput. Phys.*, vol. 375, pp. 1238–1269, 2018.

[68] V. A. Titarev and E. F. Toro, "ADER: Arbitrary high order Godunov approach," *J. Sci. Comput.*, vol. 17, no. 1–4, pp. 609–618, 2002.

[69] V. A. Titarev and E. F.Toro, "ADER schemes for three-dimensional nonlinear hyperbolic systems," *J. Comput. Phys.*, vol. 204, pp. 715–736, 2005.

[70] E. F. Toro and V. A. Titarev, "Solution of the generalized Riemann problem for advection reaction equations," *Proc. Roy. Soc. London, Ser. A*, vol. 458, pp. 271–281, 2002.

[71] M. Dumbser, D. S. Balsara, E. F. Toro, and C.-D. Munz, "A unified framework for the construction of quadrature-free one-step finite-volume and discontinuous Galerkin schemes," *J. Comp. Phys.*, vol. 227, pp. 8209–8253, 2008.

[72] D. S. Balsara, T. Rumpf, M. Dumbser, and C.-D. Munz, "Efficient, high accuracy ADER-WENO schemes for hydrodynamics and divergence-free magnetohydrodynamics," *J. Comput. Phys.*, vol. 228, pp. 2480–2516, 2009.

[73] D. S. Balsara, M. Dumbser, C. Meyer, H. Du, and Z. Xu, "Efficient implementation of ADER schemes for Euler and magnetohydrodynamic flow on structured meshes – Comparison with Runge–Kutta methods," *J. Comput. Phys.*, vol. 235, pp. 934–969, 2013.

[74] D. S. Balsara, "Higher order accurate space-time schemes for computational astrophysics – Part I – Finite volume methods," *Living Rev. Comput. Astrophys.*, vol. 3, 2017, Art. no. 2.

[75] J. S. Hesthaven and T. Warburton, in *Nodal Discontinuous Galerkin Methods: Algorithms, Analysis, and Applications*, 1st ed. New York, NY, USA: Springer, 2007.

[76] D. Sarmany, M. A. Botchev, and J. J. Vegt, "Dispersion and dissipation error in high-order Runge-Kutta discontinuous Galerkin discretisations of the Maxwell equations," *J. Sci. Comput.*, vol. 33, pp. 47–74, 2007.

[77] J. Niegemann, R. Diehl, and K. Busch, "Efficient low-storage Runge–Kutta schemes with optimized stability regions," *J. Comput. Phys.*, vol. 231, no. 2, pp. 364–372, 2012.

[78] J. H. Williamson, "Low-storage Runge-Kutta schemes," *J. Comput. Phys.*, vol. 35, no. 1, pp. 48–56, 1980.

[79] R. P. K. Chan and A. Y. J. Tsai, "On explicit two-derivative Runge-Kutta methods," *Numer. Algorithms*, vol. 53, pp. 171–194, 2010.

[80] Z. Grant, S. Gottlieb, and D. C. Seal, "A strong stability preserving analysis for multistage two-derivative time-stepping schemes based on Taylor series conditions," *Comm. Appl. Math. Comput.*, vol. 1, no. 1, pp. 21–59, 2019.

[81] S. Garain, D. S. Balsara, and J. Reid, "Comparing coarray Fortran (CAF) with MPI for several structured mesh PDE applications," *J. Comput. Phys.*, vol. 297, pp. 237–253, 2015.

Dinshaw S. Balsara received the Ph.D. degree in computational physics and astrophysics from the University of Illinois at Urbana-Champaign, Champaign, IL, USA, in 1990.

He is currently a Professor with the Department of Physics and the Department of Applied and Computational Mathematics and Statistics. He has developed computational algorithms and applications in the areas of interstellar medium, turbulence, star formation, planet formation, the physics of accretion disks, compact objects, and relativistic astrophysics. Many of the algorithms developed by him for higher order methods have seen extensive use and have been copiously cited.

Dr. Balsara was the recipient of the 2014 Department of Energy Award of Excellence for significant contributions to the Stockpile Stewardship Program and the 2017 Global Initiative on Academic Networks Award from the Government of India. He serves the community as an Associate Editor of *Journal of Computational Physics and Computational Astrophysics and Cosmology*.

Jamesina J. Simpson (Senior Member, IEEE) received the B.S. and Ph.D. degrees in electrical engineering from Northwestern University, Evanston, IL, USA, in 2003 and 2007, respectively.

She is currently an Associate Professor with the Electrical and Computer Engineering Department, University of Utah, Salt Lake City, USA. Her research laboratory encompasses the application of the Maxwell's equations finite-difference time-domain method to a wide variety of scientific and engineering applications across the electromagnetic spectrum.

Dr. Simpson was the recipient of the 2010 NSF CAREER Award, 2012 Donald G. Dudley, Jr. Undergraduate Teaching Award of the IEEE Antennas and Propagation Society, and 2017 International Union of Radio Science Santimay Basu Medal. She is currently a Track Editor for IEEE TRANSACTIONS ON ANTENNAS AND PROPAGATION.